Article

Not peer-reviewed version

Multifunctional Coatings Based on Sn, Ni and TiO_2 Aggregates with Enhanced Anticorrosion and Antibacterial Properties

Hanna Pianka , V. P. Boufal , Olga Alisiyonak , Maxim Vlasov , Alexander Chernik , Yanpeng Xue , Abdelhafed Taleb *

Posted Date: 4 September 2024

doi: 10.20944/preprints202409.0328.v1

Keywords: multifunctional coating; anticorrosion; antibacterial; Sn and Ni thin films; TiO_2 nanoparticles

Article

Multifunctional Coatings Based on Sn, Ni and TiO_2 Aggregates with Enhanced Anticorrosion and Antibacterial Properties

H. Pianka [1], V. P. Boufal [1], O. Alisiyonok [1], M. Vlasov [2], A. Chernik [1], Y. Xue [3] and A. Taleb [4,*]

[1] Belarusian State Technological University, 13a Sverdlova st, 220006 Minsk, Belarus; hanna.pianka@mail.ru (H.P), alisiyonak@belstu.by (O.A), alexachernik@gmail.com (A.C), leraboufal85@gmail.com (V. P)
[2] Institute of High Temperature Electrochemistry of the Ural Branch of the Russian Academy of Sciences, Akademicheskaya st., 20, 620066 Yekaterinburg, Russia m_vlasov@ihte.ru (M.V),
[3] National Center for Materials Service Safety, University of Science and Technology Beijing, Xueyuan Road 30, 100083, Beijing, China; yanpengxue@ustb.edu.cn (Y.X),
[4] Sorbonne université, 4 place Jussieu, 75231 Paris, France; abdelhafed.taleb@sorbonne-universite.fr (A.T)
* Correspondence: abdelhafed.taleb@sorbonne-universite.fr; Tel.: +33-1 85 78 41 97 (F.)

Abstract: Multifunctional coatings based on Sn-Ni materials with and without titanium oxide nanoparticles (TiO_2NPs) incorporation were prepared using the electrochemical deposition technique at 70°C. TiO_2NPs were dispersed in the electrolyte bath, and their influence on both surface texture, crystalline phase, and properties was investigated. Various techniques such as X-ray phase analysis (XRD), scanning electron microscopy (SEM), and energy dispersive X-ray microanalysis (EDX) were used to characterize the prepared coatings. The anti-corrosion effectiveness of the coatings was assessed using potentiodynamic polarization curves and electrochemical impedance spectroscopy in an artificial sweat medium, while the bactericidal activity of the composite coatings (the ability to induce cell death) was evaluated in accordance with ISO 27447:2009 test. The influence of the TiO_2NPs on the composition, structure and properties of the deposited coatings was established. Particular attention was paid to the relationship between the anticorrosive and bactericidal properties of the coatings and their structure and composition. The synergistic effect of the various properties was investigated and discussed.

Keywords: multifunctional coating; anticorrosion; antibacterial; Sn and Ni thin films; TiO_2 nanoparticles

1. Introduction

In recent years, there has been a growing demand for multifunctional coatings that combine physical, biological, chemical and mechanical properties, such as increased hardness, decorative appearance, corrosion resistance, hydrophobicity and antibacterial properties. Indeed, the changing conditions in which coatings are used require them to be multifunctional in order to meet the challenges and demands of their environment. Various approaches have been developed to produce coatings with different properties, making them multifunctional. Among these approaches, those that combine different chemical elements and controlled nanostructuring of the surface have proven to be very effective in producing multifunctional coatings. Alloys produced by electrochemical deposition have demonstrated their ability to exhibit multiple properties, which can lead to the multifunctional nature of certain coatings and their widespread use in industry.

Metallic coatings have evolved considerably in recent times, from single layer coatings to multi-layer gradient and micro-stack coatings, and from alloy coatings to composite coatings. The most common alloys used in coatings are nickel-based, specifically nickel-tin, which offer a wide range of properties such as corrosion, wear and abrasion resistance. To date, protective metals and alloys such as Zn [1], Ni-based alloys [2], Al-based alloys [3], Ti [4], Hf [5], Cr [6] and Cu [7] have been investigated for various applications, particularly for metals that are prone to corrosion.

 doi:10.20944/preprints202409.0328.v1

The blending of chemical elements in the composition of an alloy is a proven approach to create synergies between the individual properties of each component, which can lead to the enhancement of existing properties or the emergence of new ones [8–10]. The study of alloys of different metals and their properties is one of the main thrusts of the materials field, as is their shaping in the form of coatings.

Coatings with anticorrosive, superhydrophobic and antibacterial properties [11–14] are currently in demand for certain surfaces that require constant disinfection, such as door handles, handrails, lift buttons, etc. Cu-based electrochemical coatings are well known in the literature for their antibacterial properties and decorative appearance [15–18]. TiO_2 is another material widely reported in the literature for its photocatalytic and antibacterial properties in metal coatings [19–21]. The synthesis method and preparation conditions often determine many of the characteristics and properties of TiO_2 nanoparticles, such as size, morphology, crystalline phase, degree of agglomeration, etc. [22–25]. TiO_2 has been used as an inert phase in composite coatings based on Cu [15,16], Zn [26,27], Ni [28–32] and alloys [33–37] to impart photocatalytic and antibacterial properties. The influence of ultrasonic treatment on the electrodeposition of Cu-Sn-TiO_2NPs nanocomposite coatings with improved antibacterial properties has been studied in the literature [15]. The effect of ultrasonic treatment and current loading on the microstructure, quantitative and qualitative composition, distribution of TiO_2NP aggregates and antibacterial properties against E. coli bacteria was demonstrated. In addition, a comparative study of the effect of mechanical agitation and ultrasound on the properties of the nanocomposite coatings obtained was carried out.

Electrochemically produced Sn-Ni-based alloy coatings are widely used in metal finishing and microelectronics [38–49]. They prevent allergic skin reactions and corrosion resistance in artificial environments [43], and can replace nickel electroplating on the skin of clothing fasteners. They can also replace chromium in the decorative and lighting industries [40]. This alloy has a combination of physical and chemical properties that allow it to be widely used in industry. These include increased corrosion resistance, improved hardness, high wear resistance and many other properties [38–49]. Various electrolytes have been used to deposit Sn-Ni alloys, including fluoride chloride [34,36], pyrophosphate [39,41], sulphuric acid [42], glyconat [42] and others. Various studies have reported the influence of the kinetic parameters of Sn-Ni alloy deposition on its physicochemical and mechanical properties [40–49], as well as on composite coatings with TiO_2 NPs of different phase compositions [33–36]. Visible and photoactive Sn-Ni-TiO_2NPs electrolyte coatings incorporating carbon-doped particles and N- and S-doped TiO_2NPs (N, S-TiO_2) have been reported in the literature [34]. It has been reported that the optimum parameters for obtaining the best co-deposition rates of carbon and doped TiO_2NPs are a low current density of 1 A/dm^2 and a concentration of 30 g/1 under DC conditions. The highest co-deposition percentage of 3.25 wt% was obtained in the case of incorporation of N, S-TiO_2NPs. TiO_2 NPs synthesized by direct oxidation of titanium have been reported in the literature [35,36] and yielded a mixture of two TiO_2 polymorphs, anatase and rutile, with a particle size of 30-50 nm. The effect of the TiO_2NPs aggregate content on the physicochemical and biocidal properties of Sn-Ni coatings has been demonstrated [36].

The aim of the present work was to study the kinetics of electrochemical deposition of Sn-Ni-TiO_2NPs composite coatings, as well as the effect of the incorporation of TiO_2NPs synthesized by the hydrothermal method on their properties. The mechanism of coating formation was also investigated. The corrosion resistance of Sn-Ni-TiO_2NPs coatings prepared in an artificial sweat environment and their antibacterial properties were investigated, and the relationship between the properties of the coatings and their structure, composition and roughness was established. This will allow us to evaluate the use of these coatings for public applications such as door handles, turnstiles, lift buttons, etc.

2. Materials and Methods

The Sn-Ni alloy coating was deposited using a fluoride chloride electrolyte, with the ionic strength of the solution compensated by sodium chloride. The compositions of the solutions are given in the Table 1.

 doi:10.20944/preprints202409.0328.v1

Table 1. Electrolyte compositions used for the different coatings studied.

Component	Concentration, mol/L		
	1	2	3
$SnCl_2 \cdot 2H_2O$	0.22±0.022	0.22±0.022	–
$NiCl_2 \cdot 6H_2O$	1.05±0.021	–	1.05±0,021
NH_4F	1.35±0.135	1.35±0.054	1.35±0,054
NaCl	–	3.19±0,034	0.67±0,034

Electrolytes were prepared using double distilled water and analytical grade $NiCl_2 \cdot 6H_2O$, $SnCl_2 \cdot 2H_2O$ reagents purchased from Belreachim. NH_4F, NaCl and HCl compounds were also purchased from Belreachim. After mixing all the electrolyte components, the pH of the electrolyte was adjusted with 0.1 M HCl and 1 g/l titanium dioxide, synthesized according to the procedure described in [25], was added to the electrolyte composition. The electrolysis was carried out at a temperature of 70°C, pH of 3, current density of 1 A/dm^2 and with continuous stirring using a magnetic stirrer, and the anode consisted of nickel and tin. To avoid contamination of the electrolyte by sludge, the anode was enclosed in fabric sheaths. Copper was used as the cathode.

The kinetics of coating deposition was studied by chronovoltammetry and chronoamperometry using an Autolab PGSTAT 302N potentiostat and a three-electrode configuration consisting of a saturated silver chloride electrode as reference electrode and a platinum electrode as counter-electrode.

The most commonly used model to describe the electrocrystallization process is that of Scharifker and Hills (SH). It can be used to determine the type of nucleation by analyzing the rising parts of the chronoamperograms before the nuclei diffusion zones overlap. Depending on the slope of these parts of the chronoamperogram, two types of nucleation can be identified: instantaneous and progressive. Instantaneous nucleation corresponds to the situation where all the nucleation sites on the surface are immediately activated by the application of the potential. Furthermore, the number of nuclei remains globally unchanged during the growth process.

In the case of progressive nucleation, the number of nuclei increases progressively with deposition time. Equations (1) and (2) describe progressive and instantaneous nucleation, respectively, in the electroplating process:

$$\left(\frac{i}{i_{max}}\right)^2 = \frac{1.9542}{\frac{t}{t_{max}}}\left\{1 - exp\left[-1.2564\frac{t}{t_{max}}\right]\right\}^2 \cdot instanneous \quad (1)$$

$$\left(\frac{i}{i_{max}}\right)^2 = \frac{1.2254}{\frac{t}{t_{max}}}\left\{1 - exp\left[-2.3367\frac{t}{t_{max}}\right]^2\right\}^2 \cdot progressive \quad (2)$$

Where i_{max} is defined as the maximum current from a current transient at a corresponding time, denoted by t_{max}.

The phase composition of the coatings was determined by X-ray phase analysis (XRD) using a Bruker D8 Advance AXS diffractometer. X-ray scanning was performed at a rate of one degree per minute using CuKα radiation. The position of the maxima of the analyzed lines was measured to an accuracy of ±0.05°.

The Raman spectra were measured at room temperature on a U1000 Raman microscope-spectrometer (Renishaw, UK). The spectra were excited by laser radiation with a wavelength of 532 nm (power 5 mW on the sample). Registration was carried out with a spectral resolution of 1 cm^{-1}.

The surface morphology of the prepared coatings was studied by scanning electron microscopy (SEM) using a JEOL JSM-5610 LV microscope, while their elemental composition was determined by energy dispersive X-ray (EDX) microanalysis using a JED-2201 EDX.

 doi:10.20944/preprints202409.0328.v1

Corrosion tests were carried out in an artificial sweat medium, the composition of which is shown in Table 2.

Table 2. The composition of artificial sweat electrolyte g/L.

Compounds	NaCl	NH_4Cl	$(NH_2)_2CO$	CH_3COOH	$C_3H_6O_3$
concentration g/L	20.0	17.5	5.0	2.5	15.0

Polarization curves were recorded at a sweep rate of 1 mV/s, 20 minutes after the working electrode was immersed in the artificial sweat solution to establish a steady-state potential. Corrosion currents were calculated from the intersection of the straight Tafel sections of the cathode and anode curves. Impedance spectra were recorded in the frequency range 10 kHz to 0.01 Hz with an AC voltage amplitude of 10 mV. The impedance frequency spectra were recorded 20 minutes after the sample had been kept in the test solution. The data obtained were processed using Nova 2.1 and ZView 3.2c software.

Test cultures of the health indicator bacteria Escherichia coli ATCC 8739 and Staphylococcus aureus ATCC 6538 were used to assess the antimicrobial properties of the coatings. The antibacterial properties of the composite coatings were determined according to the standard test method ISO 27447:2009 described in the literature [35]. The evaluation of the bactericidal activity of the composite coatings in terms of their ability to induce cell death was assessed using the reduction factor (RF), which was determined using the following equation (3):

$$FR = \log(K_1/K_2) \quad (3)$$

Where, K_1, is the concentration of viable cells in the nutrient medium with the coating examined without UV irradiation (CFU/cm^3); K_2, is the concentration of viable cells in the nutrient medium with the coating examined after UV irradiation (CFU/cm^3).

3. Results

The synthesis and formation mechanism of TiO_2NPs aggregates have been described in previous works [25]. In the present work, the hydrothermal synthesis temperature was set at 170°C, and at the end of the synthesis, washing and annealing processes, a white powder was obtained. The FEGSEM characterization of the TiO_2NPs aggregate powders shows a morphology in the form of porous spherical aggregates of several particles (Figure 1a). The size of the aggregates varies from 50 to 200 nm.

 doi:10.20944/preprints202409.0328.v1

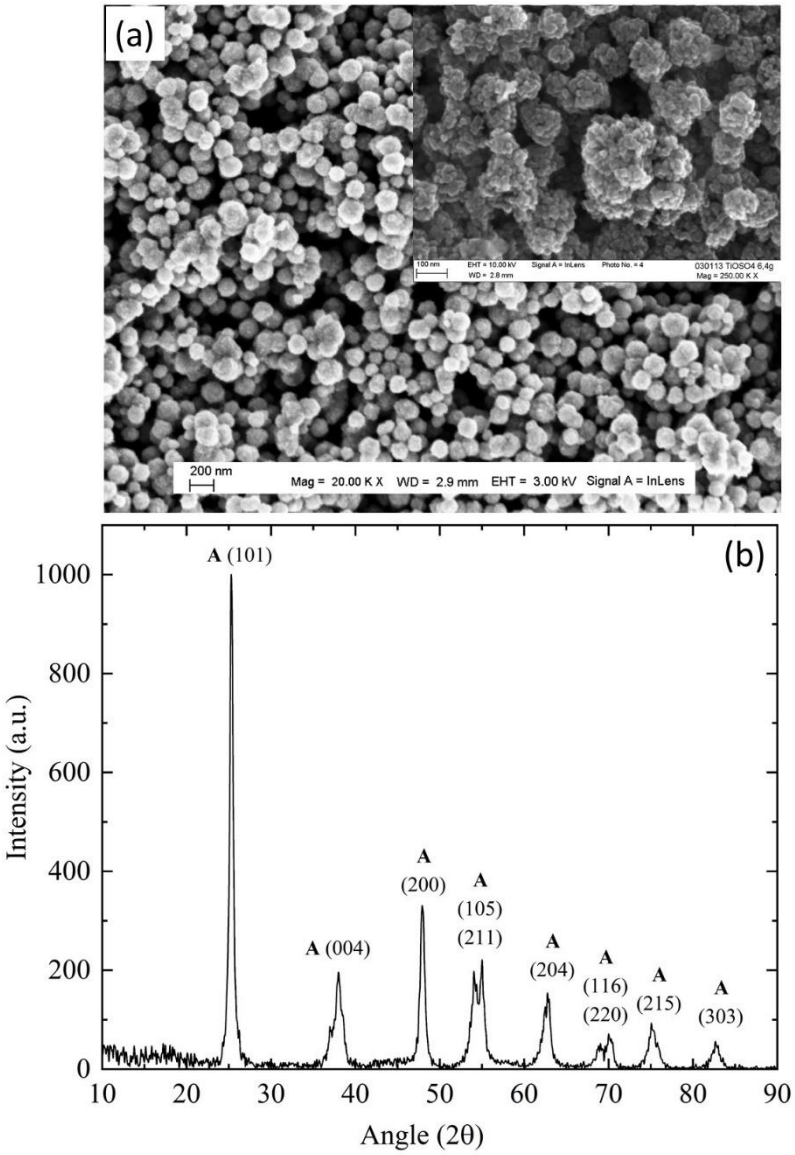

Figure 1. (**a**) FEGSEM images of TiO_2 aggregates obtained at synthesis temperatures of 170°C, insert the corresponding high magnification, (**b**) XRD pattern of TiO_2NPs aggregates prepared at synthesis temperatures 170°C.

The crystal structure and phase of the prepared TiO_2NPs aggregate powder were analyzed by X-ray diffraction. The XRD patterns obtained are shown in Figure 1b and revealed a crystal structure with peaks characteristic of the anatase phase of TiO_2NPs aggregates (JCPDS No. 89-4921). This indicates that the powder is crystallized and of high purity.

The synthesized TiO_2NPs aggregates were added to the fluoride chloride electrolyte for the deposition of the Sn-Ni alloy, as well as Ni and Sn monolayers, at a concentration of 1 g/L, as described in the experimental section. In order to understand the properties of the Sn-Ni alloy coating, a comparison was made with those of the Sn and Ni coatings. The electrochemical kinetics of the electrodeposition processes for the Sn, Ni and Sn-Ni alloy composite coatings were studied (Figure 2) with and without the addition of TiO_2NPs aggregates to the electrolyte. The electrodeposition of Sn from a fluoride chloride electrolyte with ionic strength compensation using NaCl proceeds towards potentials more negative than -0.44 V and more positive than -0.34 V for Ni. For the Sn-Ni alloy, the cathodic polarization curve shifts towards potentials more positive than the start of electrodeposition, which is around -0.28 V, indicating a depolarization effect. The

 doi:10.20944/preprints202409.0328.v1

introduction of TiO_2NPs aggregates into the electrolyte has virtually no effect on the evolution of the cathodic polarization curves of the coating deposition processes.

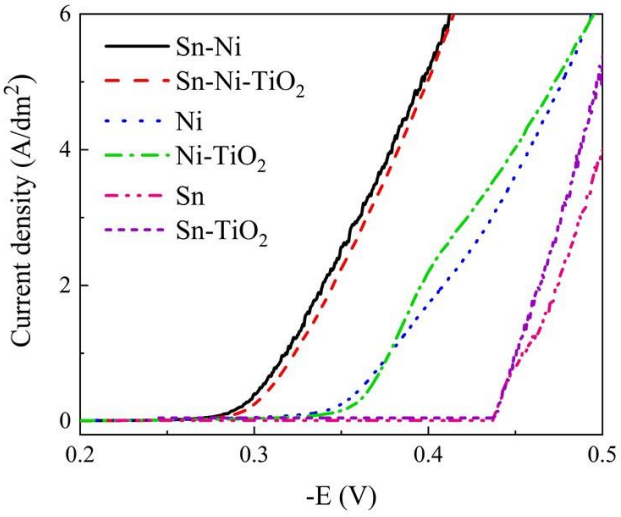

Figure 2. Cathodic polarization curves of Sn, Ni and Sn–Ni electrodeposition with and without the addition of TiO_2NPs at temperature of 70°C as indicated.

To further identify the polarization characteristics accompanying electrochemical electrodeposition reactions, the activation energy for various partial processes has been calculated (Figure 3).

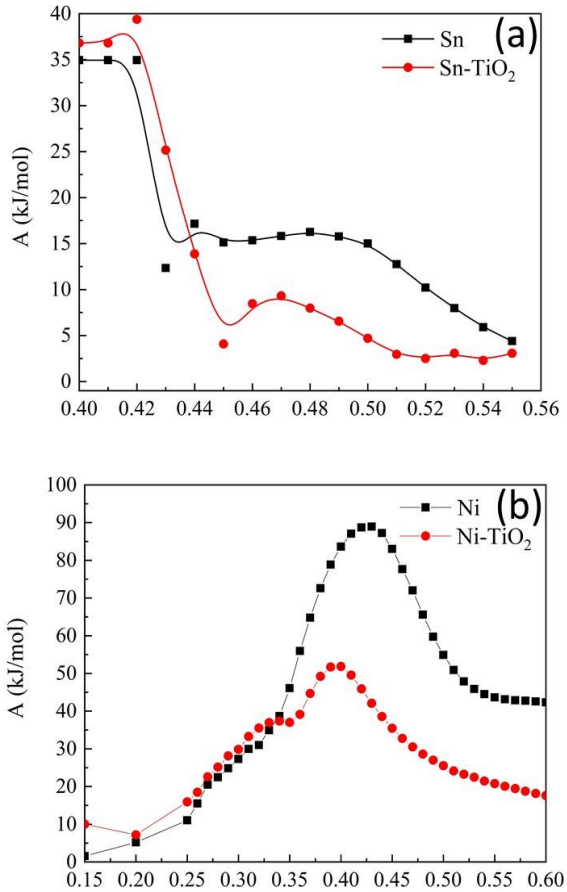

 doi:10.20944/preprints202409.0328.v1

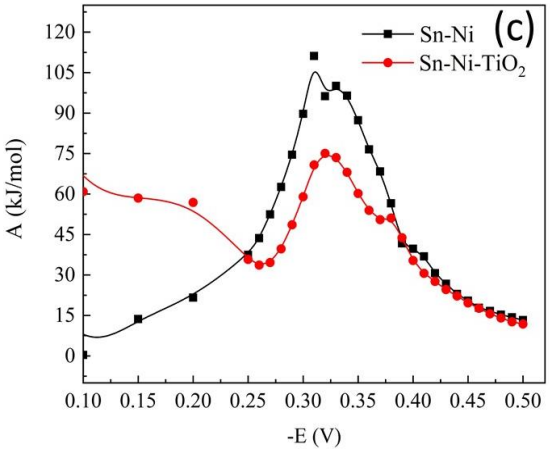

Figure 3. Dependence of the activation energy on the potential of different coatings with and without the addition of TiO_2NPs in the electrolyte as indicated.

A comparison of the activation energies of Sn and Sn-TiO_2NPs shows that in the same potential range between -0.4 and -0.44 V, the activation energies decrease uniformly. At potentials between -0.45 and -0.55 V, the variation of the activation energy shows a very slight maximum, which can be explained by a process limitation due to diffusion processes in the case of Sn and Sn-TiO_2NPs deposition, in good agreement with results published in the literature [34]. In the case of the Sn-Ni alloy coatings, a more pronounced activation energy peak is observed at -0.35 V. By comparing the dependence of the activation energy on the deposition potentials of the Sn-Ni alloy and the Sn-Ni-TiO_2NPs composite, it can be concluded that the ions are discharged together in the form of intermetallic compounds, similar results have been reported in the literature [34].

The nucleation mechanism of Sn-Ni electrodeposition was studied using the chronoamperometry technique, and the potentiostatic current-time transient curves at different potentials are shown in Figure 4a. The current peak over a short period (-230...-410 mV) is due to the formation and growth of the crystalline nuclei, then the current gradually decreases due to electron transfer and tends to a flat state at the end due to the growth of the alloy nuclei. This shows the typical characteristic of a diffusion-controlled electrochemical nucleation process with three-dimensional nucleus growth and can be characterized by the Cottrell equation, which is expressed in equation (4) as follows [29]:

$$i = \frac{n \cdot F \cdot A \cdot D^{\frac{1}{2}} \cdot c_0}{\pi^{\frac{1}{2}} \cdot t^{\frac{1}{2}}} \quad (4)$$

Where, i, is the current through the electrolyte, n is the number of electrons involved, F, is Faraday's constant, A, is the working area of the electrode, D, is the diffusion coefficient, C_o, is the concentration of the species in the bulk and, t, is time. The diffusion coefficient is an important kinetic parameter used to estimate the effect of additives on the electrodeposition of Sn-Ni and can be determined from the slope of the chronoamperogram of, i, versus, $t^{1/2}$, according to Cottrell's equation (Eq. 4).

 doi:10.20944/preprints202409.0328.v1

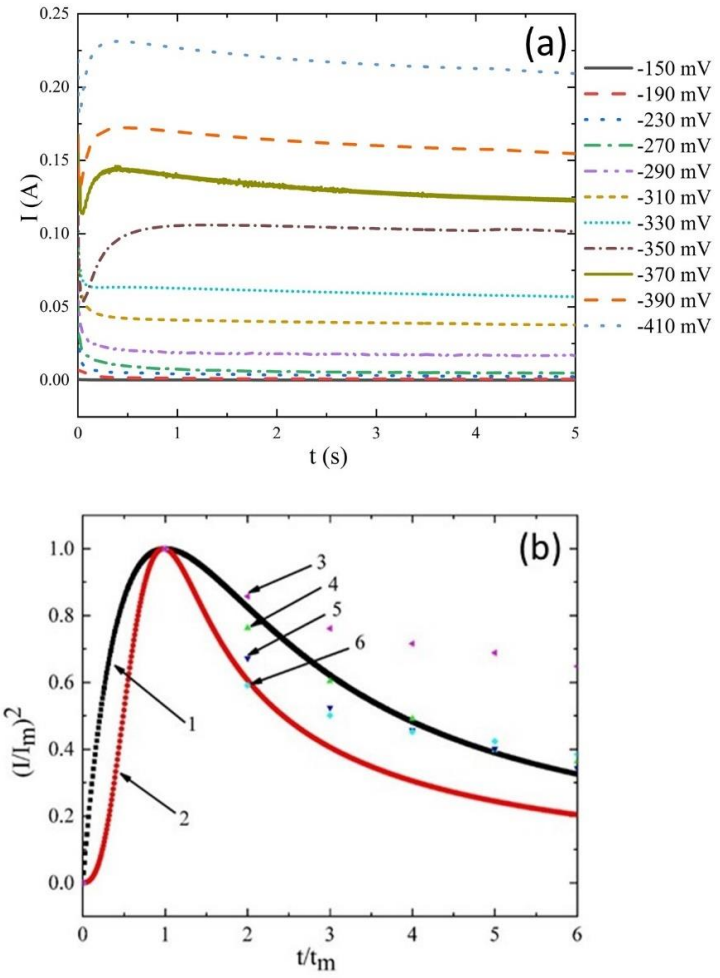

Figure 4. (**a**) Chronoamperograms of the Sn–Ni alloy deposition at various potentials, (**b**) Typical current-time transients for the electrodeposition of a Sn-Ni alloy from a fluoride-chloride electrolyte (T=70°C) at different applied potentials, V: 3) -0.250; 4) -0.310; 5) -0.320; 6) -0.390. Theoretical representations of the SH models in cases 1 - instantaneous nucleation and 2 - progressive nucleation.

It has been observed that as the potential moves towards more electronegative values down to -410 mV, the time taken to reach the maximum current on the chronoamperograms increases (Figure 4a).

A comparison of some other parameters, such as the maximum value of the transient current (I_m) and the time to reach it (t_m) for the electrodeposited alloy with different applied potentials is shown in Figure 4b. It can be seen that when the potential is more negative, the value of I_m is higher and the value of tm is greater. A comparison of the curves obtained at different potentials with the theoretical instantaneous and progressive curves of the SH model is shown in Figure 4b. This comparison shows that the experimental curves are closer to an instantaneous nucleation model; therefore, the electrodeposition of Sn-Ni follows an instantaneous nucleation mechanism and the three-dimensional growth is controlled by diffusion [39]. In addition, the deposition potential slightly affects the Sn-Ni nucleation mechanism. However, Figure 4b shows that when $t > t_m$, the experimental curves deviate from the theoretical instantaneous nucleation behavior due to proton reduction during Sn-Ni electrodeposition, which can occur during electrodeposition of metal ions in aqueous solutions as observed in previous work [41].

The SEM and EDX characterizations in Figure 5 show that within 2 seconds of electrolysis at a potential of -0.32 V, the nuclei begin to coalesce to form a continuous film, while the Ni content of the

 doi:10.20944/preprints202409.0328.v1

alloy formed is almost twice the Sn content. This could be an indication of the predominance of Ni deposition in the early stages of electrolysis.

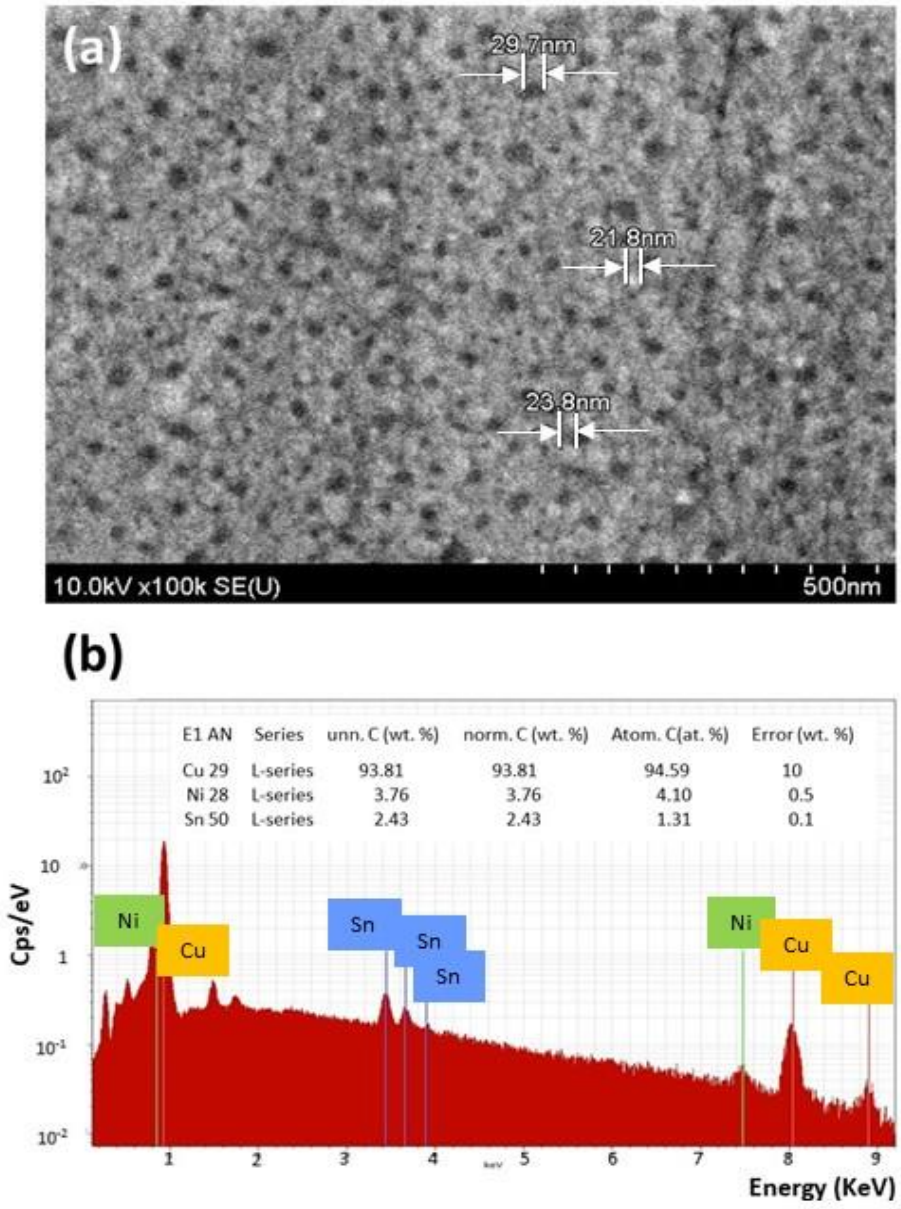

Figure 5. (**a**) SEM image of the electrode surface after Sn-Ni electrodeposition over 2 s at applied potential of - 0.32 V, and (**b**) the corresponding EDX.

Influence of Current Density on Cathode Current Efficiency

In complex electrolytes, the variation in cathodic current yield is due to the process characteristics of the electrode surface. The evolution of the cathodic current yield as a function of the applied current density for TiO_2NPs-based alloy and composite coatings at a concentration of 1 g/L is shown in Figure 6.

 doi:10.20944/preprints202409.0328.v1

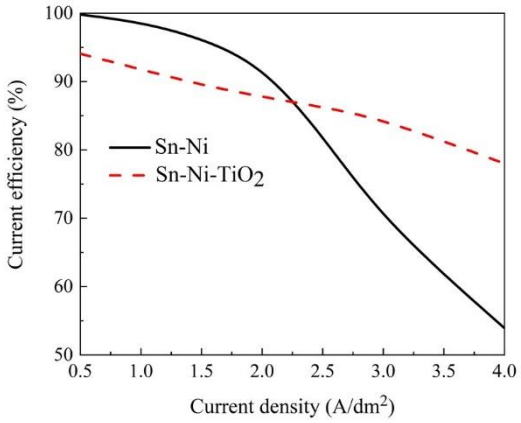

Figure 6. The current efficiency versus the current density for Sn–Ni and Sn–Ni–TiO_2 coatings.

It was found that as the current density increased from 0.5 to 4 A/dm², the cathodic current efficiency for the Sn-Ni alloy decreased from 99.8% to 53.9%. With the introduction of TiO_2NPs into the electrolyte composition, an approximately linear dependence of current efficiency on current density was observed. For a composite coating with TiO_2NPs, the current efficiency of the coating is much higher at high current densities, which may be due to an increase in electrolyte diffusion and a significant change in the composition of the coating phase. To confirm the latter hypothesis, the crystal phase and elemental composition of Sn-Ni alloy coatings at different current densities were investigated and the X-ray diffraction results are shown in Figure 7.

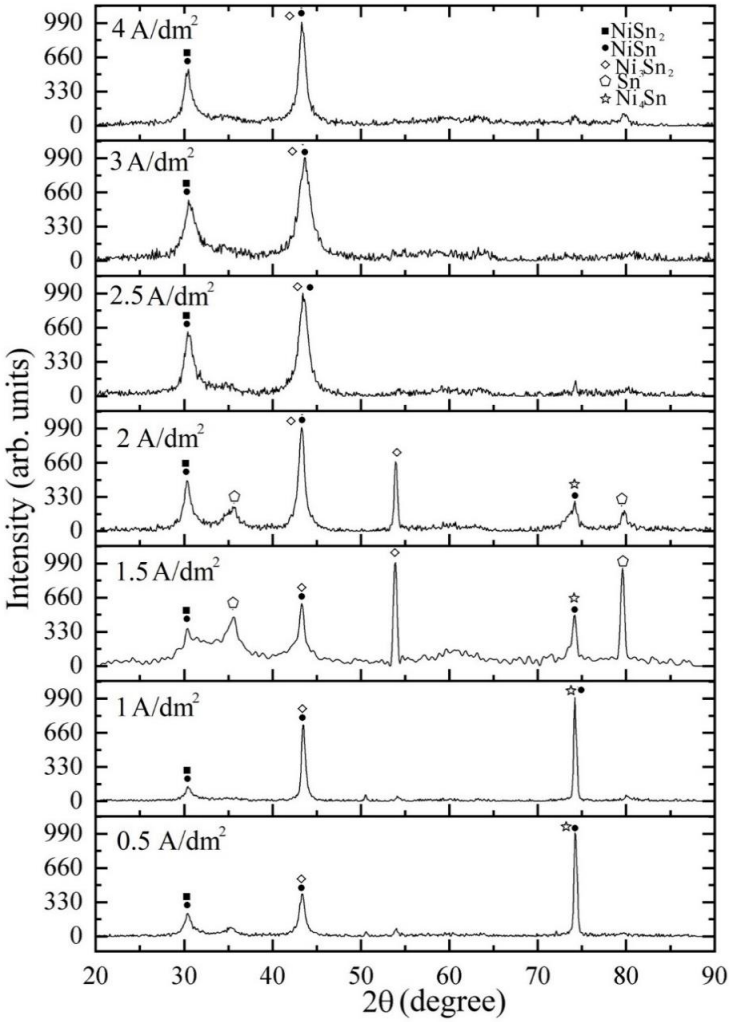

 doi:10.20944/preprints202409.0328.v1

Figure 7. XRD patterns of coatings based on Sn-Ni alloy at different current densities.

Figure 7 shows that an increase in current density to 2.5 A/dm² is accompanied by a significant change in the phase composition of the coatings. It is also interesting to note that the Ni_4Sn intermetallic compound did not form at current densities above 2.5 A/dm², whereas a Sn peak was observed for coatings deposited at current densities of 1.5 and 2 A/dm². It should be noted (Figure 8) that the Sn and Ni contents of the alloy also increase slightly with current. At current densities of 2 A/dm² and above, the Ni and Sn contents in the coating tend towards a 50/50 ratio.

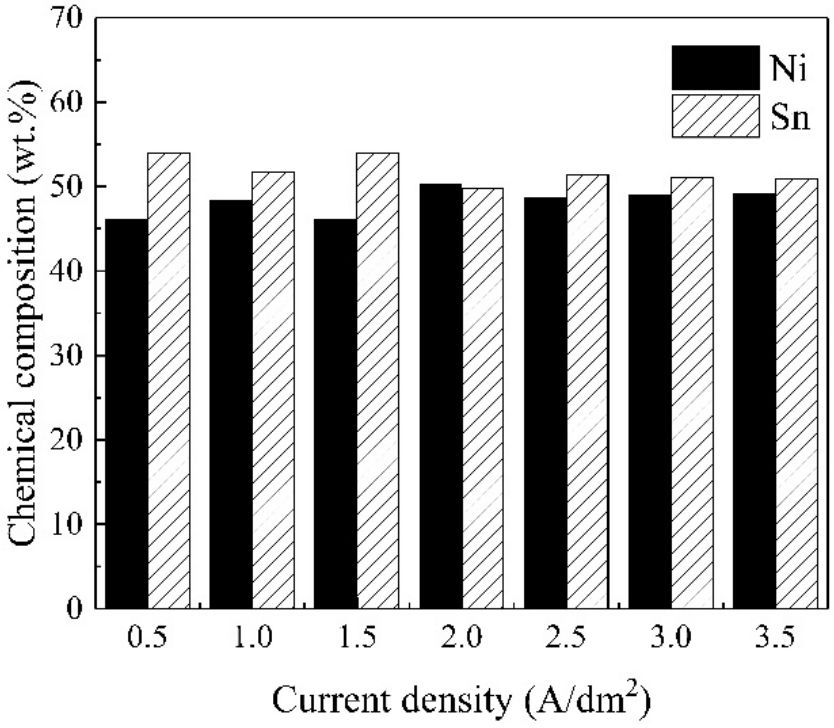

Figure 8. Elemental analysis of Sn–Ni coatings at different current densities.

Increasing the cathodic current density slightly affects the structure of the coatings and also leads to changes in the Sn/Ni ratio. The maximum Ni content in the alloy composition is observed at a current density of 2 A/dm² and amounts to 50.2 wt%, the minimum content is observed at a current density of 1.5 A/dm² and amounts to 46.06 wt%. These results show that an increase in cathodic current density induces Ni and Sn deposition in equivalent proportions. Another hypothesis to explain the behavior of current efficiency as a function of current density is the increase in the specific surface area of the electrode. Under the influence of the electric field resulting from the applied electrodeposition potential, TiO_2NPs covered with ionic adsorbates migrate towards the cathode surface where they are adsorbed. As a result, the positively charged particles adsorbed on the cathode surface increase the active surface area and provide more nucleation sites for Ni^{2+} ion reduction [50].

The Influence of TiO_2NPs Concertation on Structure and Composition of Deposited Coating Based on Sn-Ni Alloy

The introduction of TiO_2NPs into the electrolyte also contributes to a change in the composition of the coating phase.

The XRD results in Figure 9 show the presence of Cu in the structure of the Sn coatings. This may be due to the diffusion of Sn into the Cu substrate structure and the formation of intermetallic compounds. TiO_2NPs peaks are absent from the diffraction pattern, which can be explained by the relatively low concentration of TiO_2 in the composition of the electrolytes used to prepare the

 doi:10.20944/preprints202409.0328.v1

coatings. Figure 10 shows the diffractograms of the Sn-Ni alloy and the Sn-Ni-TiO2NPs alloy-based composite coating.

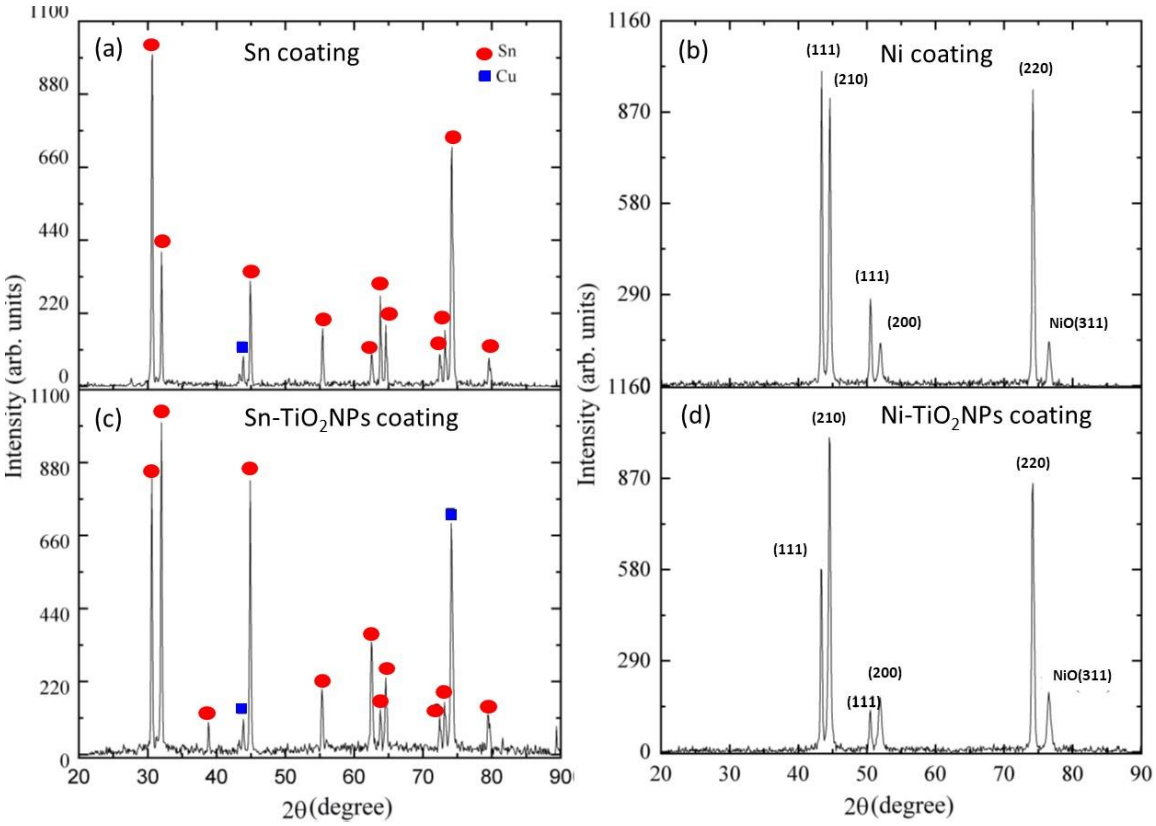

Figure 9. Diffractogram of different prepared coatings as indicated (**a**) Sn, (**b**) Ni, (**c**) Sn– TiO2NPs and (**d**) Ni–TiO2NPs.

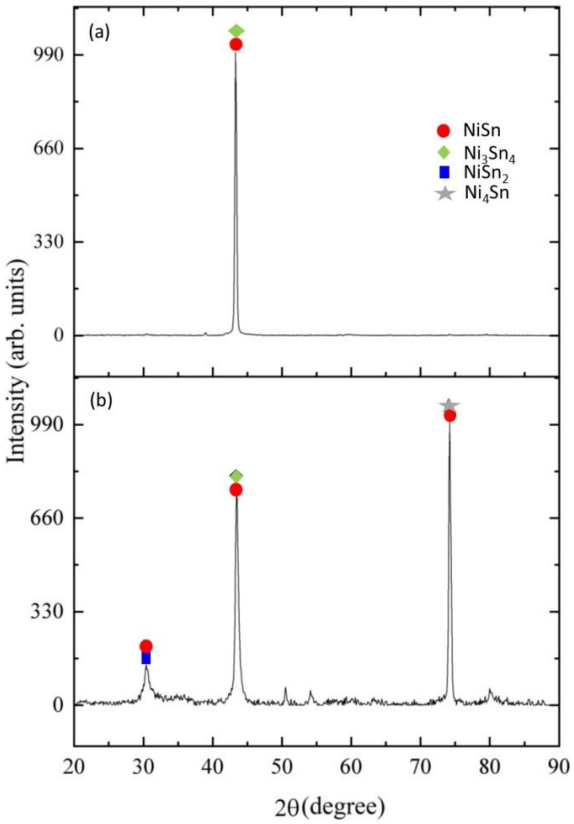

 doi:10.20944/preprints202409.0328.v1

Figure 10. Diffractograms of (**a**) Sn−Ni and (**b**) Sn–Ni TiO_2NPs coatings.

The XRD results in Figure 10 show that the Sn-Ni alloy is formed by a number of unstable intermetallic compounds such as NiSn, $NiSn_2$, Ni_3Sn_2, Ni_4Sn. When TiO_2NPs are introduced into the electrolyte, the intensity of the main NiSn metastable peak changes. This can be explained by a slight change in the Sn content associated with a change in its solubility. The structure of the prepared coatings was also studied by SEM and the results are shown in Figure 11.

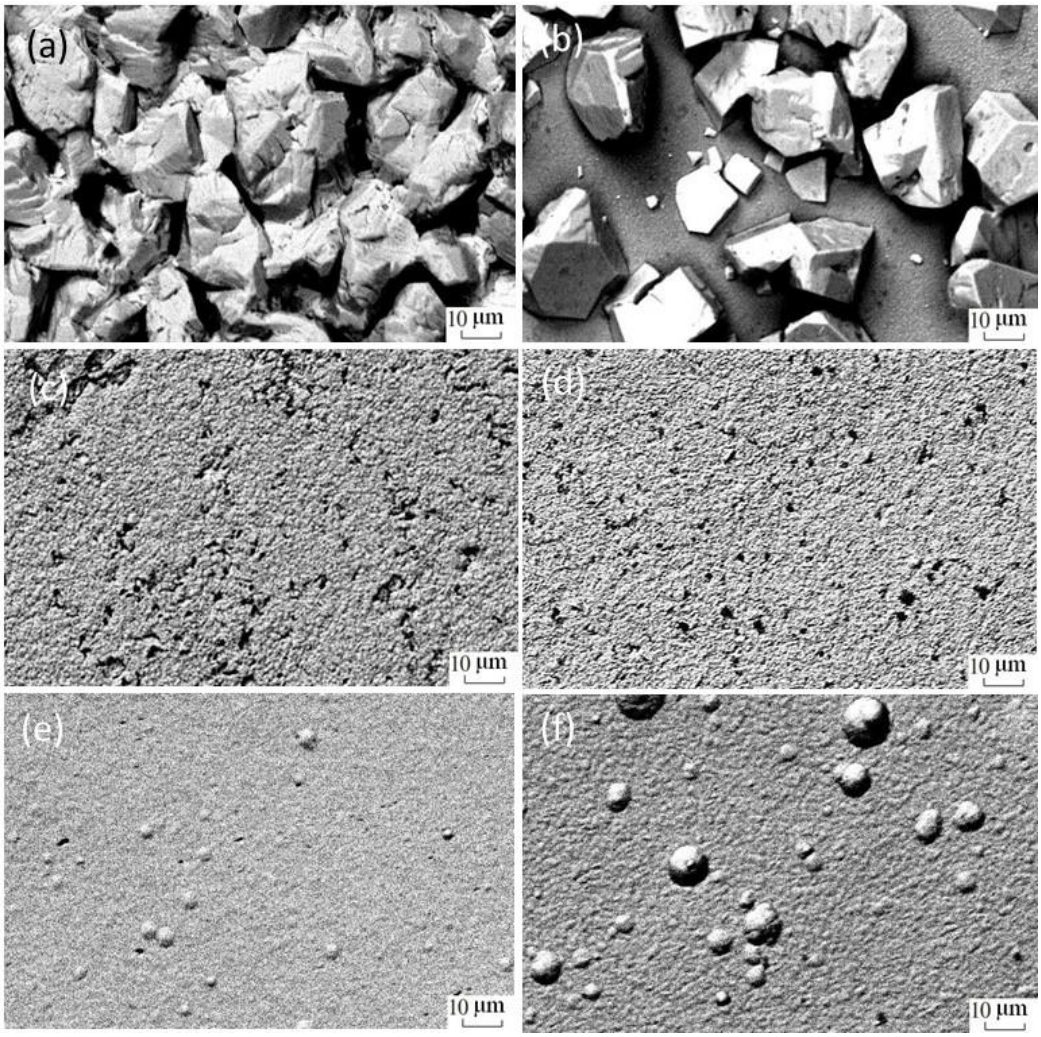

Figure 11. SEM images of different prepared coatings (**a**) Sn, (**b**) Sn–TiO_2NPs, (**c**) Ni, (**d**) Ni–TiO_2NPs, (**e**) Sn–Ni and (**f**) Sn–Ni TiO_2NPs, at current density of 1A/dm^2.

The introduction of TiO_2NPs into the electrolyte leads to changes in the texture of the prepared coatings. It has been shown that in the case of Sn-TiO_2NPs deposition, more pronounced facet structures are observed compared to Sn deposition (Figure 11a,b). The Sn-TiO_2NPs coating is inhomogeneous with the local formation of large Sn-TiO_2NPs about 20 µm larger than the Sn grains (Figure 11a) and larger than the size of the TiO_2NP aggregates (Figure 1a). This may be due to the hindered deposition of the Sn coating when the large TiO_2NPs aggregates are deposited on the substrate surface, as well as the rapid diffusion of Sn into the Cu substrate with the formation of new intermetallic compounds. In the case of Ni, when the TiO_2NPs are introduced into the electrolyte, the deposit has a uniform texture with fewer pores (Figure 13d). The Sn-Ni alloy coating is characterized by the formation of small spheroidal crystallites (Figure 11e). When TiO_2NPs are introduced into the electrolyte composition during the deposition of the Sn-Ni alloy, an increase in the size of the spheroids on the surface is observed, reaching diameters of the order of 10 µm larger than the size of

 doi:10.20944/preprints202409.0328.v1

the TiO_2NPs aggregates (Figure 1a), which is the signature of local inclusion of TiO_2NPs in the coating (Figure 11f). The elemental and phase compositions of the prepared alloys and coatings are given in Table 2.

Table 2. Composition of different prepared coatings based on Sn, Ni, Sn–Ni alloy without and with TiO_2NPs.

Coating	Element	composition, mas. %
1	2	3
Sn	Sn	100
Sn $TiON_2Ps$	Sn	38.38
	Cu	60.47
	TiO_2	0.73
Ni	Ni	100
Ni $TiON_2Ps$	Ni	99.87
	TiO_2	0.13
Sn–Ni	Sn	51.69
	Ni	48.31
Sn–Ni $TiON_2Ps$	Sn	55.78
	Ni	44.22
	TiO_2	0

For single metal coatings, the Cu content reaches 100%. In the case of Sn-TiO_2NPs, the coating is characterized by an irregular structure and the intercrystallite contain Cu (Figure 11d). In addition, it has been shown that when TiO_2NPs at a concentration of 1 g/L are introduced into the Sn and Ni deposition electrolytes with ionic strength compensation, the TiO_2NPs are incorporated into the Sn and Ni coatings with a composition limit of 0.73 and 0.13 wt.%, respectively. For the Sn-Ni alloy coating, the Sn and Ni contents are 51-56 wt.% and 48 wt.%, respectively. In the case of the composite alloy coating, TiO_2NPs are not present in the coating composition. This may be due to their very inhomogeneous inclusion in the coating composition in the form of agglomerates of TiO_2NPs aggregates. As the EDX analysis did not reveal the presence of TiO_2NPs in the coating, an XRF analysis was carried out for confirmation (Table 3).

Table 3. Elemental content of all coatings.

Coating	Element	composition, mas. %
Sn–Ni	Ni	32.31
	Sn	67.66
	Cl	0.03
Sn–Ni TiO_2NPs (1 g/l)	Ni	46.19
	Sn	53.77
	Cl	0.04
	Ti	0
Sn–Ni–TiO_2NPs (2 g/l)	Ni	37.26
	Sn	62.59
	Cl	0.03
	Ti	0.12

Table 3 shows that Ti was not detected in the Sn-Ni TiO_2NPs based coating at a TiO_2NPs concentration of 1 g/l in the electrolyte. However, by increasing the TiO_2NPs concentration to 2 g/l in

 doi:10.20944/preprints202409.0328.v1

the electrolyte, the Ti content in the coating increases to 0.12 wt.%, a signature that TiO_2NPs have been incorporated into a Sn-Ni TiO_2NPs based coating. To further investigate the presence of TiO_2NPs in the Sn-Ni TiO_2NPs coating, Raman experiments were carried out and the spectra are shown in Figure 12. Analysis of these spectra provided an estimate of the TiO_2NPs content.

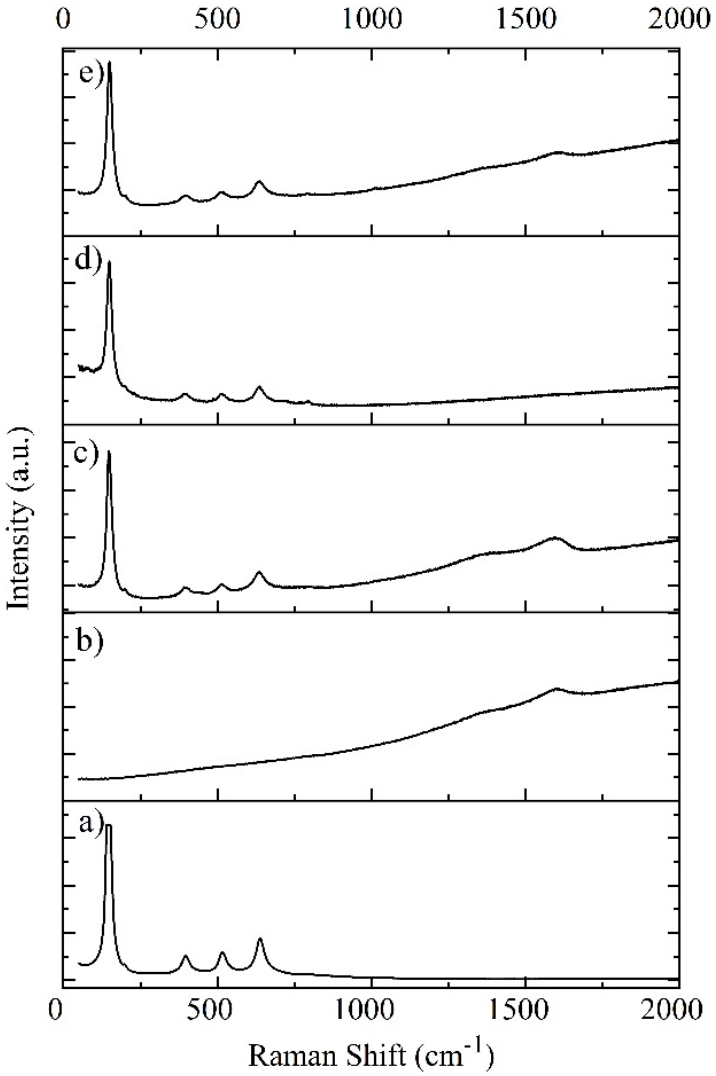

Figure 12. Raman spectra for TiO_2NPs (**a**), Sn-Ni (**b**) and composite coatings based on Sn-Ni alloy with different concertation of TiO_2NPs in electrolyte (g/l): 1 (**c**), 2 (**d**) and 5 (**e**).

In the Raman spectra corresponding to Sn-Ni alloy based composite coatings with the presence of TiO_2NPs in the deposition electrolyte, peaks were observed in the region of 150, 395, 512, 634 cm^{-1} (Figure 12c,e), which are characteristic of TiO_2NPs (Figure 12a). This confirms the inclusion of TiO_2NPs in the composition of Sn-Ni alloy based composite coatings and that the embedded TiO_2NPs increase with the concentration of TiO_2NPs in the electrolyte. In addition, these results show that Raman measurements are more sensitive to the presence of TiO_2NPs in Sn-Ni alloy based composite coatings at concentrations lower than 1g/l.

Furthermore, the introduction of TiO_2NPs into the composition of the deposition electrolyte for Sn, Ni and Sn-Ni coatings was observed to have an ambiguous effect on the surface roughness of the prepatterned coatings (Figure 13).

 doi:10.20944/preprints202409.0328.v1

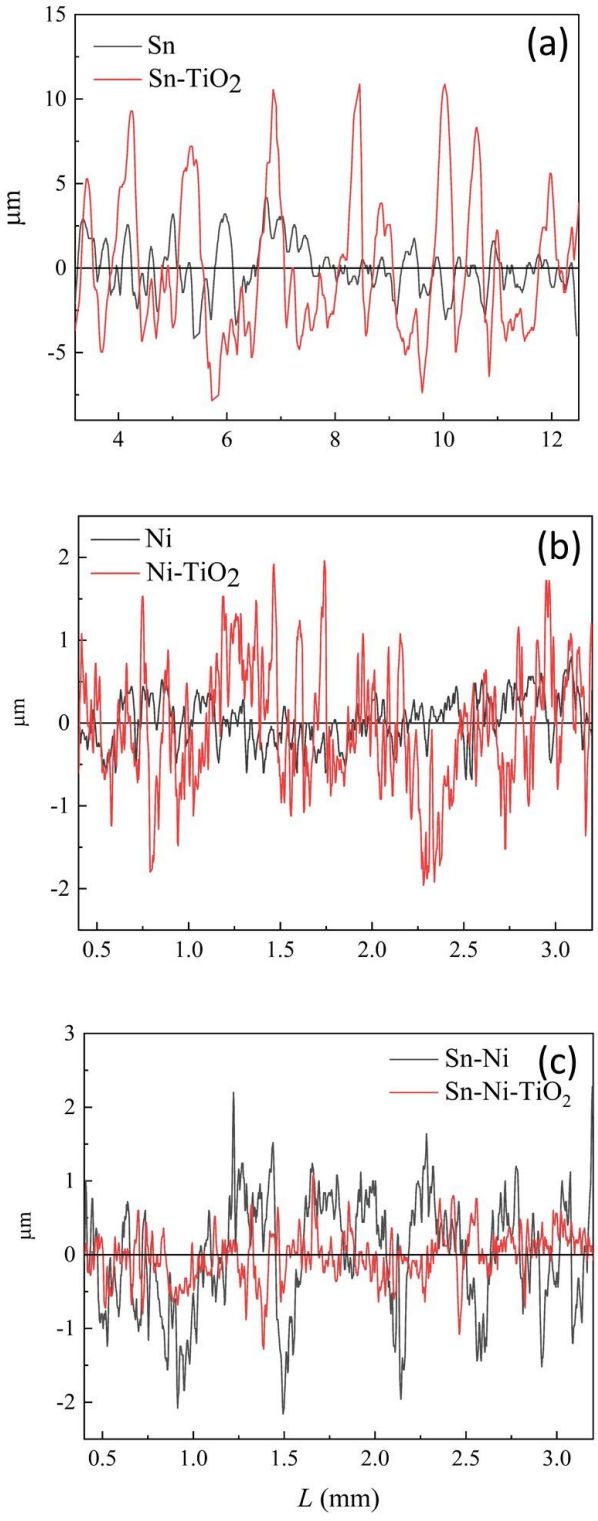

Figure 13. Microroughness of (**a**) Sn, (**b**) Ni and (**c**) Sn-Ni coatings with and without TiO_2NPs.

With the introduction of TiO_2NPs into the deposition electrolyte composition, Sn and Ni coatings become rougher. However, for a Sn-Ni alloy based composite coating, the microroughness decreases slightly. This can be explained by the uniform incorporation of TiO_2NPs into the alloy phase deposited over the entire surface, as well as the absence of TiO_2NPs agglomeration in the deposition electrolyte. Table 4 shows the surface microroughness for the different coatings studied.

Preprints.org (www.preprints.org) | NOT PEER-REVIEWED | Posted: 4 September 2024 doi:10.20944/preprints202409.0328.v1

Table 4. The main indicators of the microroughness of the surface of different prepared coatings.

Coating	Ra, µm	Rz, µm	Rmax, µm
Sn	1.14	5.24	7.89
Sn–TiO_2NPs	3.54	13.11	20.73
Ni	0.21	1.04	1.37
Ni–TiO_2NPs	0.58	3.05	3.94
Sn–Ni	0.41	2.02	3.45
Sn–Ni–TiO_2NPs	0.34	1.66	2.97

It was found that by introducing 1 g/l TiO_2NPs in the composition of the electrolyte for the deposition of Sn and Ni (with compensation of the ionic strength by a NaCl solution), the various parameters quantifying microroughness (R_a, R_{max} and R_z) increased by almost three times. In the case of composite coatings based on Sn-Ni-TiO_2NPs alloys, the opposite effect was observed, i.e. a decrease in roughness. The dependence of the microroughness of Sn-Ni coatings on the deposition current density was also investigated and the results are shown in Figure 14.

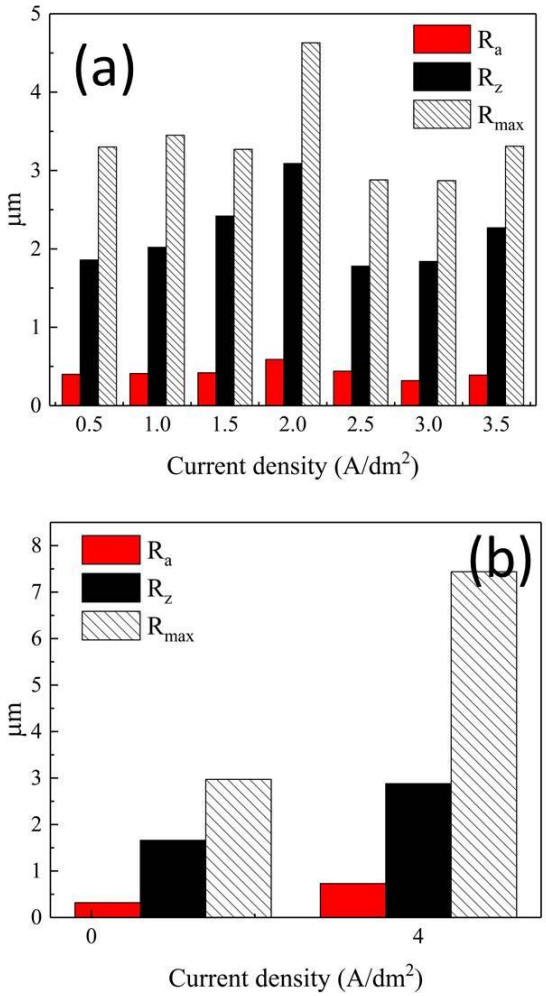

Figure 14. Microroughness of the surface of Sn-Ni coatings (**a)** at different current densities, (**b**) Sn-Ni-TiO_2NPs coating (CEC) at current densities 1 and 4 A/dm^2. .

The roughness results shown in Figure 14 (a) indicate that maximum values of R_a, R_z and R_{max} were obtained at a current density of 2 A/dm^2 while minimum values were observed at a current density of 3 A/dm^2. The irregular dependence of microroughness on current density may be related

 doi:10.20944/preprints202409.0328.v1

to a significant change in phase composition and degradation of coatings deposited at current densities above 3 A/dm². In the case of TiO_2NPs-based composite coatings, the evolution of microroughness was studied at current densities of 1 and 4 A/dm² and the results are shown in Figure 14 (b). It can be observed that an increase in the current density of Sn-Ni-TiO_2NPs coatings leads to an increase in the roughness parameters R_a, R_{max} and R_z by a factor of 2 to 3. These results are in good agreement with those obtained from the SEM characterization. In fact, the textures observed from the SEM characterization show an increase in the size of spheroids on the surface, which is a signature of local inclusion of TiO_2NPs in the coating.

Surface roughness is a characteristic that has a major influence on the properties of the coating, particularly its optical and wetting properties. The physical interaction of a liquid with the surface of a solid or other liquid determines the wetting properties of that surface, and the degree of wetting is characterized by the wetting contact angle, θ, which is the angle formed by the plane tangent to the interfacial surfaces bounding the wetting liquid, with the vertex of the angle lying on the line of separation of the three phases. Depending on this angle, a distinction is made between hydrophilic ($\theta < 90°$) and hydrophobic ($\theta > 90°$) surfaces. The value of the contact angle (θ), excluding the effect of gravity, depends solely on the molecular properties of the solid surface and the phases in contact with it. Figure 15 shows a diagram of the effect of current density on the wetting angles of Sn-Ni alloy coatings.

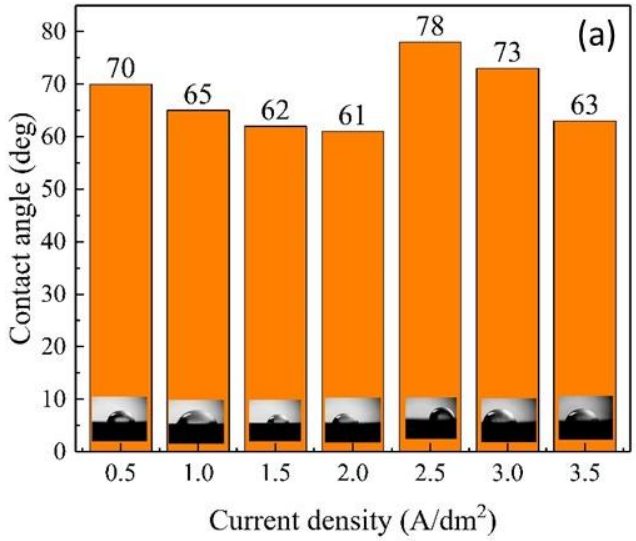

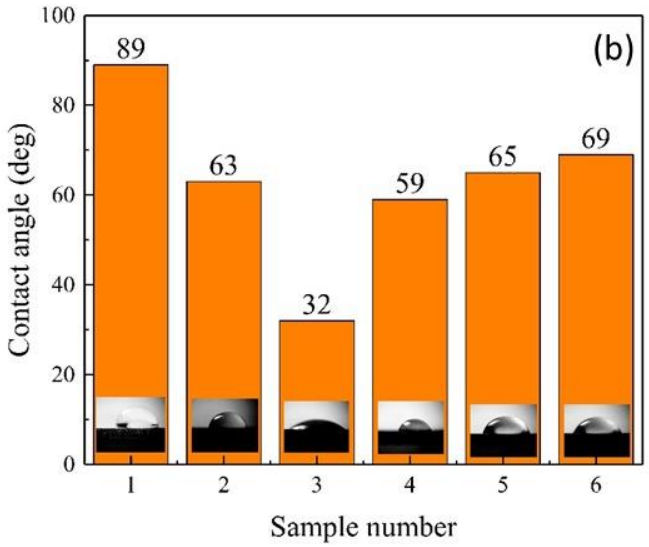

 doi:10.20944/preprints202409.0328.v1

Figure 15. Contact angle of the (**a**) Sn-Ni coating at different current densities, (**b**) studied coatings, 1 – Sn, 2 – Sn–TiO_2NPs, 3 – Ni, 4 – Ni–TiO_2NPs, 5 – Sn–Ni and 6 – Sn–Ni–TiO_2NPs.

In Figure 15a the results show that the variation in contact angle is inversely proportional to the variation in surface roughness. For coatings with the lowest roughness, obtained at a current density of 2.5 A/dm², the maximum value of the wetting angle was observed to be 78°±1.2. For Sn-Ni alloy-based coatings with higher roughness, obtained at a current density of 2 A/dm², the wetting contact angle reached minimum values of around 61°±1.3°. Furthermore, the introduction of TiO_2NPs into the composition of the deposition electrolyte of Sn or Ni or Sn-Ni based coatings contributes to a modification of the wetting contact angle (Figure 15b).

As well as affecting surface roughness, the introduction of TiO_2NPs also contributes to changes in the composition and structure of the coatings. TiO_2NPs introduced into the electrolyte composition for the deposition of Sn-based coatings result in a 1.4-fold decrease in contact angle. For Ni and Sn-Ni alloy coatings, the introduction of TiO_2NPs into the electrolyte composition increases the contact angle by 2 and 1.1 times respectively. The dependence of the Sn-Ni alloy wetting contact angle on the microroughness of the coatings studied was determined. The optimum current density of 1/dm² was used to obtain a wetting contact angle of about 65±1.2°. The dependence of the TiO_2NPs incorporation on the contact angles of the prepared coatings was evaluated. It was found that the introduction of 1 g/l TiO_2NPs into the composition of the Sn-Ni alloy deposition electrolyte imparts hydrophobic properties to the surface.

Corrosion Properties

Since these coatings can modify objects in massive contact with human skin, evaluation of their corrosion resistance in artificial sweat was carried out using electrochemical impedance spectroscopy. The impedance spectra in an artificial sweat medium (pH=7) are shown in Figure 16.

From the Nyquist and Bode diagrams in Figure 16, it is clear that in the absence of TiO_2NPs in the composition of Sn coatings, higher resistance values are observed. The charge transfer resistance (low-frequency region) of Sn coatings is $1.40 \cdot 10^4$ Ω·cm², however, with the introduction of TiO_2NPs, the resistance decreases to $7.90 \cdot 10^3$ Ω·cm² (Table 5). An opposite behavior was observed with the introduction of TiO_2NPs into the electrolyte composition for Ni deposition, an increase in the charge transfer resistance of the coating from $8.3 \cdot 10^3$ to $2.10 \cdot 10^4$ Ω·cm² was observed. In the case of Sn-Ni alloy-based coatings, with the introduction of TiO_2NPs, charge transfer resistance decreases from $4.25 \cdot 10^4$ to $3.7 \cdot 10^4$ Ω·cm². The impedance spectra were analyzed using the equivalent circuit shown in the insert of Figure 16a. The parameters obtained from simulation of the impedance spectra using the equivalent circuit are shown in Table 5.

Table 5. Parameters of the equivalent circuits of the impedance spectra for coatings Sn, Ni, Ni–Sn and Sn–TiO_2NPs, Ni–TiO_2NPs, Sn–Ni TiO_2NPs obtained in an artificial sweat medium.

Coating	R_s (Ω cm²)	R_1 (Ω cm²)	Y_1 (Ω^{-2} cm^{-2}s^n)	n_1	R_2 (Ω cm²)	Y_2 (Ω^{-2} cm^{-2}s^n)	n_2
Sn	18.74	11300	$1.53\ 10^{-5}$	0.8	3000	$5.93\ 10^{-4}$	0.5
Sn–TiO_2NPs	5.03	7450	$5.03\ 10^{-5}$	0.78	1000	$4.43\ 10^{-4}$	0.15
Ni	12.53	6277	$1.9\ 10^{-4}$	0.8	832,9	$1.77\ 10^{-5}$	0.79
Ni–TiO_2NPs	13.57	19277	$7.93\ 10^{-5}$	0.7	3833	$5.16\ 10^{-5}$	0.89
Sn–Ni	11.5	33053	$4.98\ 10^{-5}$	0.91	9896	$7.96\ 10^{-5}$	0.62
Sn–Ni–TiO_2NPs	18.04	25067	$3.65\ 10^{-5}$	0.79	8891	$5.13\ 10^{-5}$	0.51

 doi:10.20944/preprints202409.0328.v1

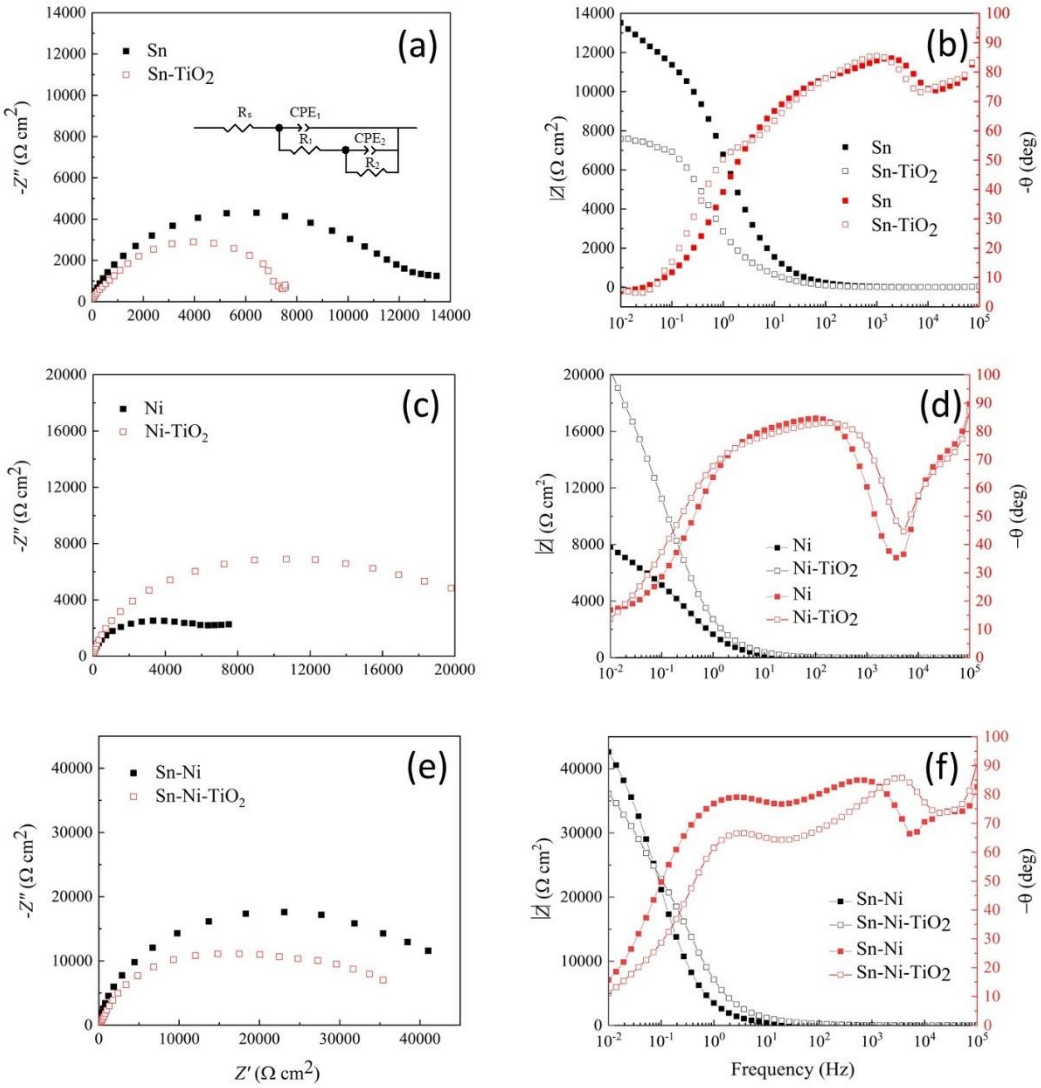

Figure 16. Nyquist and Bode diagrams of different prepared coatings as indicated in an artificial sweat medium (**a**) Sn and Sn-TiO_2NPs (Nyquist), (**b**) Sn and Sn-TiO_2NPs (Bod), (**c**) Ni and Ni-TiO_2NPs (Nyquist), (**d**) Ni and Ni-TiO_2NPs (Bod) and (**e**) Sn-Ni and Sn-Ni-TiO_2NPs (Nyquist) and (f) Sn-Ni and Sn-Ni-TiO_2NPs (Bod). The (**a**) insert correspond to Equivalent circuit of an electrochemical cell for modeling impedance spectra. R_s - solution resistance, CPE_1 - capacitive type constant phase element, R_1 - charge transfer resistance at the interface, CPE_2 - diffusion type constant phase element, R_2 - diffusion resistance.

Introducing TiO_2NPs into the electrolytes when depositing Sn and Sn-Ni coatings reduces the charge transfer resistance at the interface, whereas For Ni coatings, the introduction of 1 g/L TiO_2NPs into the electrolyte composition doubles the charge transfer resistance. For all the coatings studied, the introduction of TiO_2NPs into the deposition electrolyte composition results in a slight decrease in the exponent n1 of the CPE1 element, with values between 0.7 and 0.91, indicating the capacitive nature of the element.

To further assess the anti-corrosion properties of the prepared coatings, the potentiodynamic polarization technique was applied, and the results obtained are shown in Figure 17. The results analysis using Tafel equation yield the corrosion current and potential.

 doi:10.20944/preprints202409.0328.v1

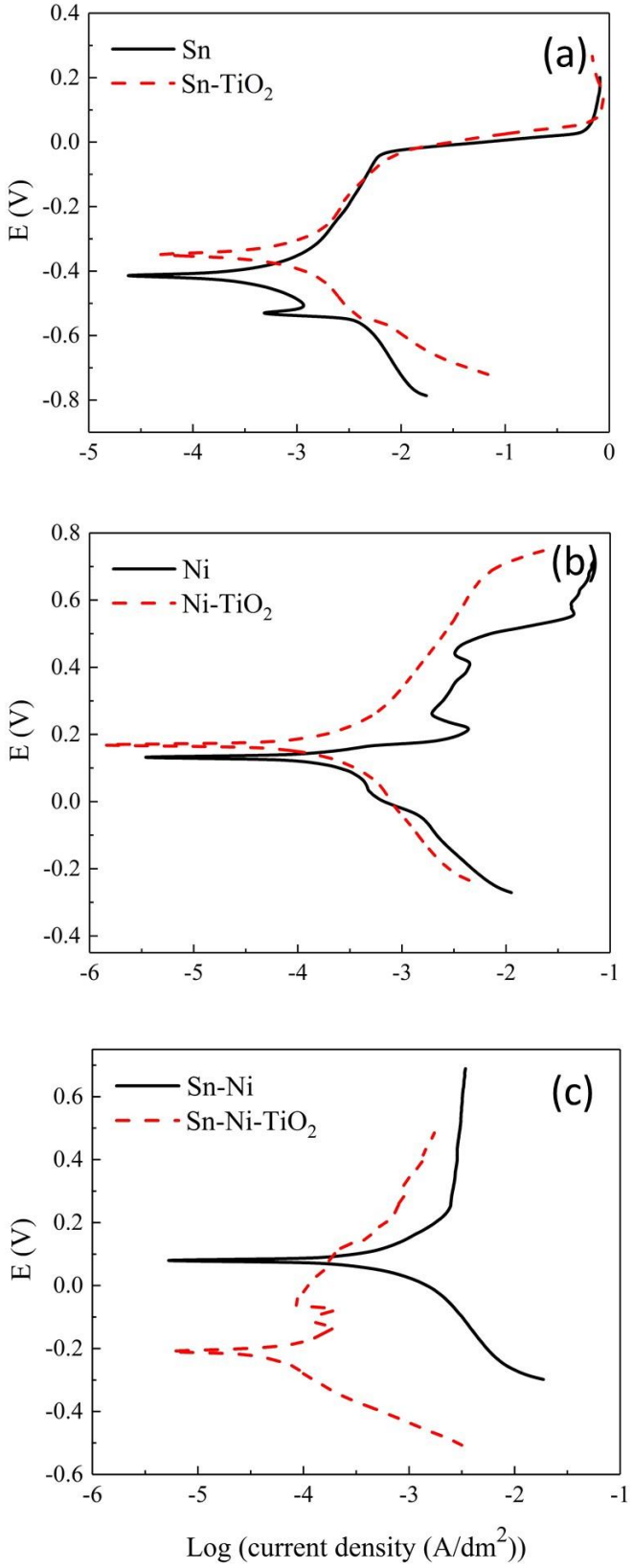

Figure 17. Potentiodynamic polarization curves of the corrosion process in an artificial sweat media of different prepared coating as indicated.

 doi:10.20944/preprints202409.0328.v1

The introduction of TiO_2NPs into the deposition electrolyte of the Sn-based coating induces a shift in corrosion potential (E_{corr}) by 70 mV towards the electropositive region, from E_{corr} (Sn) = -0.42 V to E_{corr} (Sn-TiO_2NPs) = -0.35 V, whereas this shift is only about 40mV in the case of a Ni coating. The E_{corr} increased from 0.14 V for the Ni coating to 0.18 V for the Ni-TiO_2NPs coating. In the latter case, corrosion currents (I_{corr}) are 4.84 10^{-6} A/cm^2 and 4.87 10^{-5} A/cm^2 respectively. Figure 17c shows that in the case of the Sn-Ni alloy coating, the introduction of TiO_2NPs into the electrolyte during deposition of the Sn-Ni alloy coating induces a shift of the E_{corr} by 300mV towards the electronegative region, taking the E_{corr} from 0.09 V (Sn-Ni) to -0.21 V (Sn-Ni-TiO_2NPs), the corresponding I_{corr} are $1.82 \cdot 10^{-4}$ A/cm^2 and $2.63 \cdot 10^{-5}$ A/cm^2 respectively. The results of the main corrosion process parameters in an artificial sweat environment with a pH of 7 are presented in Table 6.

Table 6. Electrochemical parameters of corrosion of the studied samples.

Coating	i_{corr} (A/cm^2)	E_{corr} (V)	a_a (V)	b_a (V)	$\lvert a_c \rvert$ (V)	$\lvert b_c \rvert$ (V)
Sn	$1.36 \cdot 10^{-4}$	-0.42	0.20	0.06	0.64	0.06
Sn–TiO_2NPs	$1.17 \cdot 10^{-4}$	-0.35	0.21	0.04	0.46	0.03
Ni	$4{,}84 \cdot 10^{-5}$	0.13	0.23	0.02	0.03	0.04
Ni–TiO_2NPs	$4.87 \cdot 10^{-5}$	0.17	0.39	0.05	0.10	0.06
Sn–Ni	$1.82 \cdot 10^{-4}$	0.08	0.36	0.08	0.16	0.06
Sn–Ni–TiO_2NPs	$2.63 \cdot 10^{-5}$	-0.2	0.06	0.03	0.67	0.10

The E_{corr} of Sn- or Ni-based coatings changes insignificantly with the introduction of TiO_2NPs into the electrolyte composition, while in the case of Sn-Ni-based coatings, the corrosion current decreases 6.9-fold. The results of electrochemical impedance spectroscopy of the coatings in a 3% NaCl solution are shown in Figure 18. It can be seen that the Nyquist diagrams obtained for all the coatings studied in the NaCl medium are characterized by a capacitive semicircle in the high- and mid-frequency region.

In the case of Ni-based coatings it can be seen in Figure 18a,b, that the introduction of TiO_2NPs into the electrolyte used for deposition, induces a higher increase in charge transfer resistance from $1.80 \cdot 10^4$ to $4.0 \cdot 10^4$ Ω·cm^2. Whereas, the Bode diagrams (Figure 18d) show a slight increase in charge transfer resistance from $1.10 \cdot 10^4$ to $1.20 \cdot 10^4$ Ω ·cm^2, in the case of Sn-based coatings with embedded TiO_2NPs (low-frequency region). For Sn-Ni alloy-based coatings (Figure 18e,f), the introduction of TiO_2NPs into the deposition electrolyte, the charge transfer resistance decreases from $1.20 \cdot 10^5$ to $9.0 \cdot 10^4$ Ω cm^2. The parameters obtained from the equivalent circuit analysis of the impedance spectra are shown in Table 6.

Table 6. Parameters of equivalent circuits used to analyze the impedance spectra of different prepared coatings (Sn, Ni, Sn-Ni and Sn-TiO_2NPs, Ni-TiO_2NPs, Sn-Ni-TiO_2NPs) in solution 3% NaCl.

Coating	R_s, (Ω cm^2)	R_1, (Ω cm^2)	Y_1, (Ω^{-2} cm^{-2}s^n)	n_1	R_2, (Ω cm^2)	Y_2, Ω^{-2} (cm^{-2}s^n)	n_2
Sn	7.89	10188	$3.6\ 10^{-5}$	0.61	1465	$1.7\ 10^{-6}$	0.77
Sn-TiO_2NPs	11.89	11324	$3.3\ 10^{-5}$	0.82	1024	$5.15\ 10^{-5}$	0.86
Ni	11.62	21679	$1.95\ 10^{-4}$	0.76	1918	$1.24\ 10^{-5}$	0.33
Ni-TiO_2NPs	13.42	44679	$6.95\ 10^{-5}$	0.74	4118	$1.42\ 10^{-5}$	0.43
Sn-Ni	11.98	145600	$3.91\ 10^{-5}$	0.8	18286	$5.57\ 10^{-5}$	0.64
Sn-Ni-TiO_2NPs	12.58	75240	$3.7\ 10^{-5}$	0.82	30001	$8.99\ 10^{-5}$	0.78

 doi:10.20944/preprints202409.0328.v1

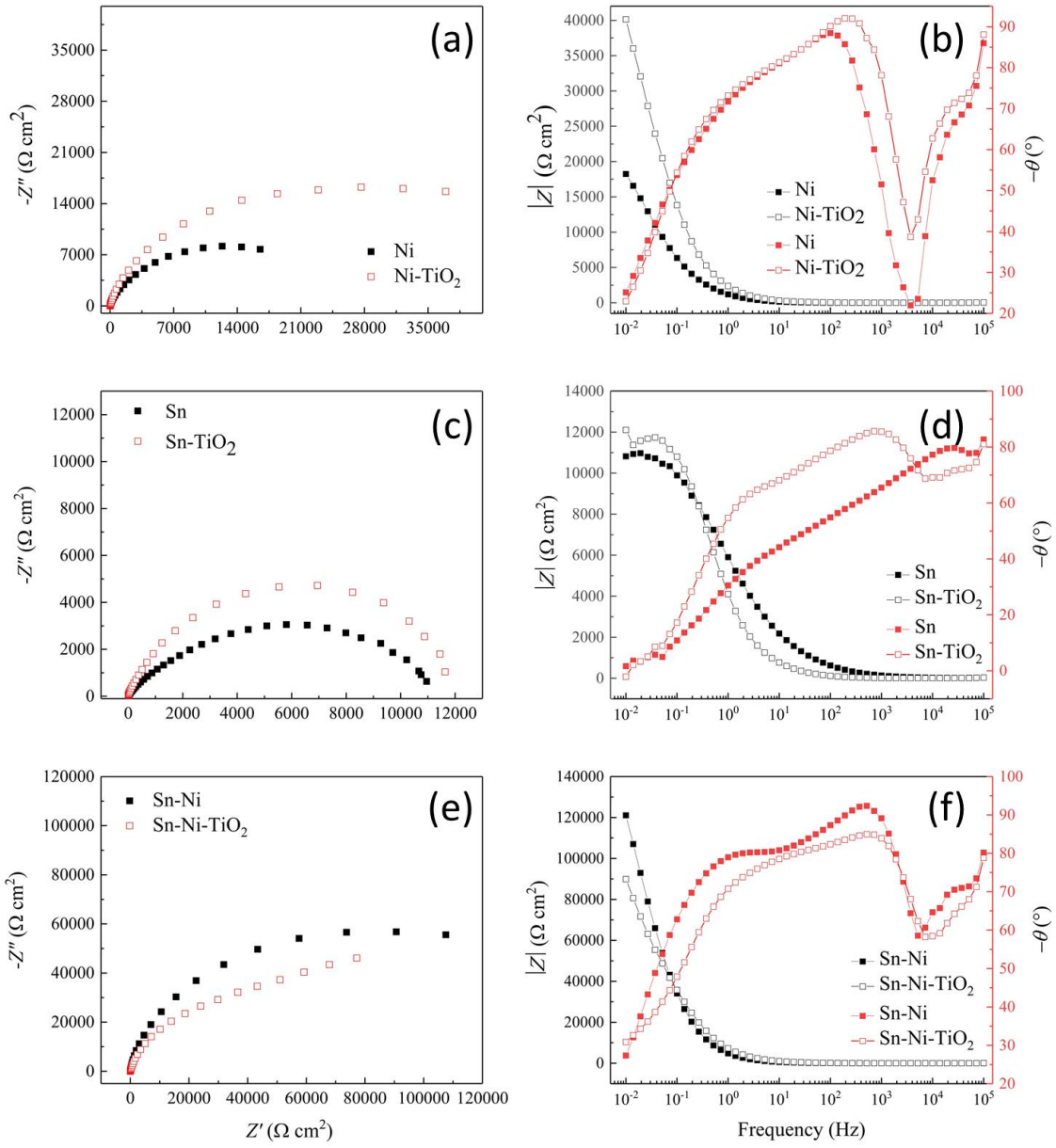

Figure 18. Nyquist and Bode diagrams of different prepared coatings in 3% NaCl solution as indicated (Ni and Ni-TiO_2NPs, Sn and Sn-TiO_2NPs, Sn-Ni alloy and Sn-Ni-TiO_2NPs).

The introduction of TiO_2NPs into electrolytes for the deposition of Ni and Sn coatings increases the resistance to charge transfer at the interface. For a Sn-NiTiO_2NPs composite coating with 1 g/L TiO_2NPs in the electrolyte composition, the charge transfer resistance indicators decrease by a factor of two. For nickel coatings, the introduction of TiO_2NPs into the composition of the deposition electrolyte decreases the exponent n of the CPE_1 element slightly, but for Sn-TiO_2NPs and Sn-Ni-TiO_2NPs this exponent increases. The n_1 index is in the range from 0.61 to 0.82, which indicates the presence of defects in the coating.

The results of potentiodynamic polarization curves are presented in Figure 19 for different prepared coatings. Based on these results, the corrosion currents and the corrosion initiation potential were calculated.

 doi:10.20944/preprints202409.0328.v1

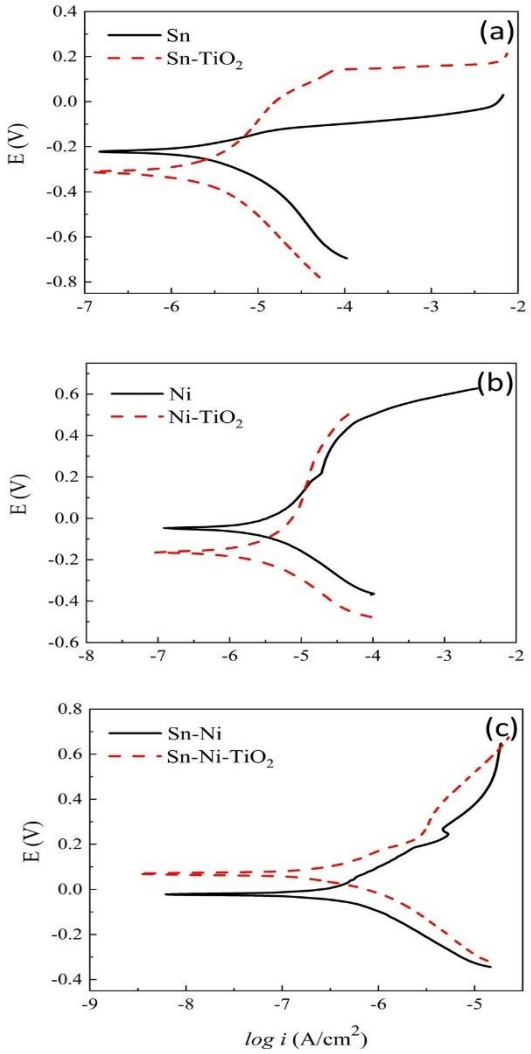

Figure 19. Potentiodynamic polarization curves of the corrosion process in a solution of 3% NaCl for prepared coatings as indicated. (**a**) Sn and Sn-TiO_2 coatings, (**b**) for Ni and Ni-TiO_2 coatings and (**c**) Sn-Ni and for Sn-Ni-TiO_2 coatings.

Analysis of the potentiodynamic polarization curves showed that the corrosion potential of the Sn-based coating (Figure 19a) is -0.22 V, and that the introduction of TiO_2NPs into the electrolyte composition for deposition resulted in a 110 mV shift in potential towards the electronegative potentials region, reaching a value of -0.33 V. It can also be observed that the corrosion current is $1.03 \cdot 10^{-4}$ A/cm^2 and $6.48 \cdot 10^{-5}$ A/cm^2 for Sn and Sn-TiO_2NPs, respectively. In the case of Ni coatings, it was observed that the corrosion potential is 0.05 V, but when TiO_2NPs nanoparticles are introduced into the deposition electrolyte, the corrosion initiation potential shifts by 230 mV towards the electronegative potentials region and reaches a value of -0.18 V. The corrosion currents corresponding to the Ni or Ni-TiO_2NPs based coatings are $2.39 \cdot 10^{-5}$ A/cm^2 and $2.18 \cdot 10^{-5}$ A/cm^2 respectively (Figure 19b). Figure 19c shows that TiO_2NPs introduced into the Sn-Ni alloy deposition electrolyte shifts the corrosion initiation potential by 100 mV towards the electropositive potentials, from 0.08 V to -0.02. Furthermore, the corrosion currents are $1.01 \cdot 10^{-4}$ A/cm^2 and 9.94 10^{-6} A/cm^2, for Sn-Ni and Sn-Ni-TiO_2NPs respectively. The main parameters characterizing the corrosion process are shown in Table 7.

 doi:10.20944/preprints202409.0328.v1

Table 7. Electrochemical Tafel parameters of corrosion of the studied coatings.

Coating	i_{corr}, A/cm^2	E_{corr}, V	a_a, B	b_a, B	$\lvert a_k \rvert$, B	$\lvert b_k \rvert$, B
Sn	$1.03 \cdot 10^{-4}$	-0.22	0.048	0.066	0.606	0.098
Sn–TiO_2	$6.48 \cdot 10^{-5}$	-0.33	0.145	0.112	0.601	0.066
Ni	$2.39 \cdot 10^{-5}$	0.05	0.483	0.095	0.792	0.181
Ni–TiO_2	$2.18 \cdot 10^{-5}$	-0.18	0.025	0.032	0.378	0.044
Sn–Ni	$1.01 \cdot 10^{-5}$	-0.02	0.18	0.04	0.298	0.056
Sn–Ni–TiO_2	$9.95 \cdot 10^{-6}$	0.08	0.33	0.051	0.329	0.081

The introduction of TiO_2NPs into the deposition electrolyte compositions of all coatings was accompanied by a more or less pronounced decrease in corrosion current. The corrosion current of Sn-Ni alloy and Ni-based coatings does not change significantly with TiO_2NPs in the deposition electrolyte composition. In the case of Sn coatings, the corrosion current decreases by a factor of 1.6.

According to these results, obtained both in an artificial sweat medium and in a 3% NaCl solution, the different coatings prepared show different trends in terms of anticorrosion properties when TiO_2NPs are added. Indeed, TiO_2NPs incorporated in Sn, Ni and Sn-Ni coatings modify their anticorrosion properties, which can be explained by their surface wetting properties and their chemical composition. As shown by SEM surface characterization, the surface texture changes with the introduction of TiO_2NPs, which consequently influences their roughness and wetting properties. It is well known in the literature that a surface with an increased contact angle reduces the area of contact with the liquid on its surface, which can lead to a reduction in the surface area in contact with the aggressive medium and therefore its corrosion [51,52]. Bearing this in mind, the results obtained can be explained as follows.

In the case of the Sn coating, the decrease in corrosion resistance can be explained by the decrease in the contact angle and therefore an increase in the surface area exposed to corrosion. Furthermore, the increase in corrosion resistance of the Ni-based coating after the incorporation of TiO_2NPs is due to the synergistic effect between the increase in contact angle, and therefore minimization of the contact surface with the aggressive solution, and the anticorrosive property of the chemical element Ni. In the case of the Sn-Ni based coating, it was observed that the corrosion resistance decreased after the introduction of TiO_2NPs, despite a relatively high contact angle compared to the other coatings and the presence of the chemical element Ni. This can be explained by the appearance of porosity in the coating after the incorporation of TiO_2NPs, which can facilitate the penetration of the aggressive solution through the coating, reaching a maximum surface area susceptible to corrosion.

Antibacterial properties are strongly recommended for surfaces in public areas that come into contact with human skin. TiO_2NPs is a material with high photocatalytic properties and, when used in coatings, imparts antibacterial properties. The antibacterial properties of the coatings prepared in this work have been investigated and are presented in Table 8.

 doi:10.20944/preprints202409.0328.v1

Table 8. Antibacterial activity of samples in relation to the test culture St. aureus ATCC 6538.

Sample	Concentration of bacterial cells C (CFU/ml)		Reduction factors (RF)
	Under UV irradiation	Without UV irradiation	
Sn–Ni (control)	$3.3 \cdot 10^3$	$1.4 \cdot 10^6$	2.6
Sn–Ni–TiO_2NPs	$2.0 \cdot 10^1$	$5.0 \cdot 10^5$	4.4
Ni	$7.0 \cdot 10^1$	$1.3 \cdot 10^6$	4.3
Ni–TiO_2NPs	$4.0 \cdot 10^1$	$9.9 \cdot 10^5$	4.4
Sn	$3.0 \cdot 10^1$	$4.4 \cdot 10^5$	4.1
Sn–TiO_2NPs	$2.0 \cdot 10^1$	$1.1 \cdot 10^6$	4.7
Sn–Ni–TiO_2NPs (Degussa)	$8.0 \cdot 10^1$	$1.6 \cdot 10^5$	3.3

According to the antibacterial test presented in Table 8, the prepared coatings show bactericidal activity with an RF parameter >2; and show that under UV light they can reduce the concentration of microorganisms by 4 to 5 orders of magnitude. Furthermore, the antibacterial activity of Sn-based coatings is due to the presence of copper with antibacterial properties in the coating composition, as Sn has no antibacterial properties. Figure 20 shows the antibacterial properties of the coatings studied in relation to the St. aureus disease test bacterium.

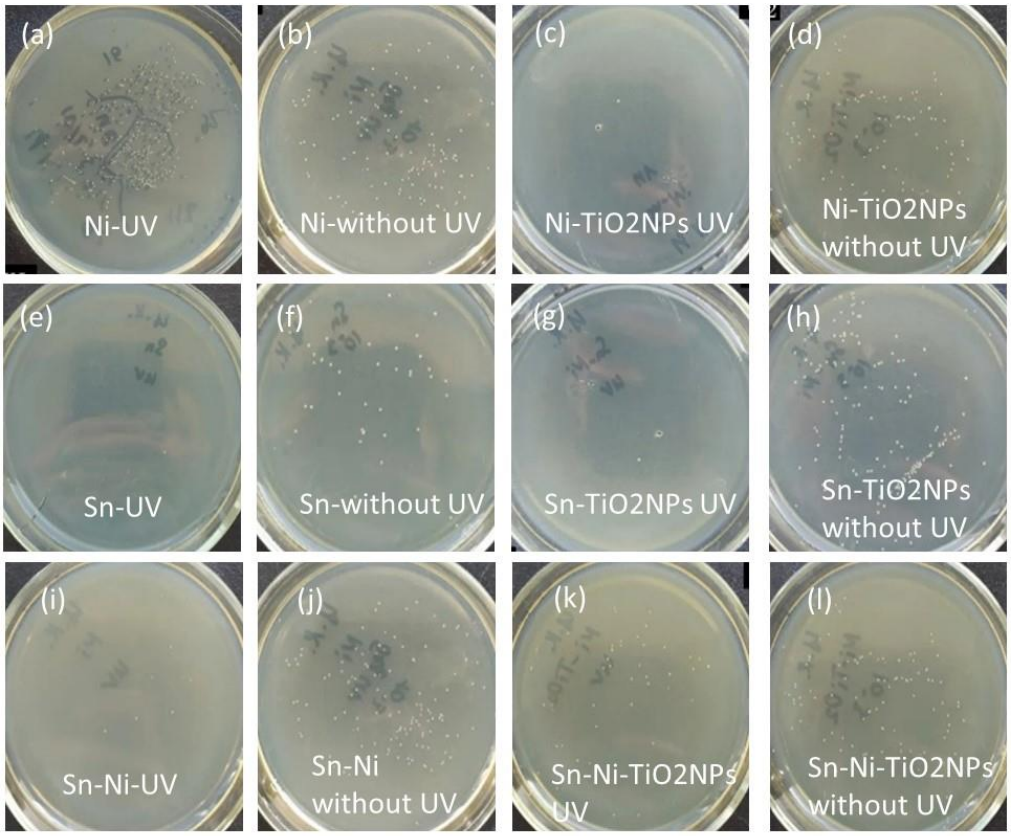

Figure 20. Antibacterial properties in terms of the bacteria St. aureus test of different prepared coating as indicated with and without UV exposition.

Experiments have shown that for all coatings, the introduction of TiO_2NPs into the composition of the deposition electrolytes, and consequently into the coatings, leads to an enhancement of the biocidal properties with and without UV radiation.

Table 9 shows that the introduction of TiO_2NPs (1 g/l) into the deposition electrolyte for the deposition of Sn, Ni, Sn-Ni coatings leads to an increase in the antibacterial properties in the presence of UV radiation for an E. coli ATTC 8739 strain, but with a lower efficacy than that observed against

 doi:10.20944/preprints202409.0328.v1

the St. John's bacterium. Electrochemical composite coatings with TiO_2NPs were shown to have the best biocidal properties against gram-positive and gram-negative strains. They can be widely used on objects that are accessible to humans in public environments.

Table 9. Results of the antibacterial activity of samples against E. coli ATTC 8739 test culture.

Sample	Concentration of bacterial cells C, CFU/ml		Reduction factors (RF)
	Under UV irradiation	Without UV irradiation	
Sn–Ni (control)	$5.4\ 10^3$	$3.9\ 10^5$	1.9
Sn–Ni–TiO_2	$3.4\ 10^2$	$9.0\ 10^4$	3.4
Ni	$3.6\ 10^2$	$1.5\ 10^5$	2.6
Ni–TiO_2	$6.0\ 10^1$	$2.5\ 10^5$	3.6
Sn	$1.9\ 10^2$	$4.6\ 10^4$	2.3
Sn–TiO_2	$1.6\ 10^3$	$5.9\ 10^5$	2.6
Sn–Ni–TiO_2 (Degussa)	$8.0\ 10^1$	$2.5\ 10^5$	3.4

In order to assess the antibacterial properties of a solid surface, several factors must be taken into account, such as the properties of the surface in terms of hydrophobicity, roughness and chemical composition, as well as the bacterial species. In fact, the proliferation of bacteria on a solid surface is affected by the configuration and roughness of the surface, which has a strong influence on the adhesion of bacteria to the solid surface and their viability. Bacterial attachment to solid surfaces is considered to be the first step in bacterial growth and proliferation. It has been widely demonstrated that poor bacterial adhesion to the solid surface leads to bacterial death. Therefore, weakening bacterial adhesion is considered one of the indirect approaches to prevent bacterial proliferation. In fact, surface patterning and roughness can increase the hydrophobic character of the surface, causing bacteria to repel and weakly adhere to the solid surface, leading to their death.

Another approach to the surface to prevent bacterial proliferation, which is considered to be direct, is the chemical composition of the surface. The metallic surfaces of nanoparticles (NPs) such as zinc, aluminum, nickel, zirconium, cerium, magnesium and titanium dioxide have antibacterial properties [53–58]. In particular, the photoelectrochemical and photocatalytic properties of TiO_2 nanoparticles [58,59] have been shown to enable them to generate electron-hole pairs that can react with water or oxygen to produce reactive oxygen species (ROS) such as superoxide anions, hydrogen peroxide and hydroxyl radicals. The latter species can penetrate bacterial cell walls and cause cell death by disrupting cell function [60–66]. Several studies in the literature have reported that TiO_2 has strong antibacterial and antifungal activity against many Gram-positive bacteria such as Staphylococcus aureus and Gram-negative bacteria such as Escherichia coli [67,68].

In addition, Ni nanocrystals have been reported to have antibacterial activity against Gram-positive/negative bacteria and bacterial spores such as Staphylococcus aureus (S. aureus) and Escherichia coli (E. coli). Although the mechanism of the antibacterial effect of Ni nanocrystals is not yet fully understood, it has been reported that during the interaction between the Ni surface and bacteria, Ni^{2+} leaching has been detected, which penetrates the bacterial membrane and generates reactive oxygen species, leading to disruption of its function and bacterial death [69]. In the case of the Sn surface, it has been reported to exhibit weak antibacterial activity when exposed to Staphylococcus aureus (S. aureus) or Escherichia coli (E. coli) bacteria [70].

To understand the antibacterial test results of the coating prepared with and without TiO_2NPs, it is necessary to consider the synergistic effect of the two factors influencing the antibacterial activity of the solid surface mentioned above. In fact, there is a synergistic effect between the surface repulsion and weakening of adhesion due to the hydrophobicity of the surface on the one hand and the antibacterial properties of the chemical elements of the solid surface on the other. In the case of Sn with low antibacterial activity, the observed result could be explained by the hydrophobicity of the

 doi:10.20944/preprints202409.0328.v1

surface leading to weak adhesion of the bacteria and their death at a later stage. When TiO_2NPs are incorporated into the Sn coating, although the contact angle decreases from 89° to 63° and therefore the adhesion of bacteria to the surface increases, the antibacterial activity of TiO_2NPs offsets this effect, explaining the small variation in RF from 2.3 to 2.6.

For Ni and Sn-Ni coatings, the strong increase in RF after incorporation of TiO_2NPs could be explained by the synergistic effect of the antibacterial properties of Ni and TiO_2NPs rather than the poor adhesion of bacteria to the surface. For the Ni coating, although the surface is hydrophilic (contact angle of 32°) and bacteria need to adhere well, the Ni guarantees the antibacterial activity of the coating. Furthermore, for the Sn-Ni coating after the incorporation of TiO_2NPs, the contact angle shows little variation (Figure 15) and therefore a similar bacterial adhesion strength, the antibacterial activity observed is mainly due to the synergistic effect between that of Ni and that of TiO_2NPs.

These results clearly show that Sn, Ni and TiO_2NPs are crucial elements to be used for the preparation of coatings with high performance anti-corrosion and antibacterial properties, as Sn-Ni-TiO_2 exhibits the best antibacterial activity with an RF of 3.4 and the best anti-corrosion performance with an E_{corr} more shifted (0.08V) towards the positive potential, a lower I_{corr} of $9.95\text{-}10^{-6}$ A/cm² and a higher charge transfer resistance of 25067 Ω·cm².

4. Conclusions

In this work it was found that the electrochemical deposition of monolayers and Sn-Ni alloy proceeds according to an instantaneous nucleation mechanism with ion transfer as the limiting step. Furthermore, it was observed that the introduction of TiO_2NPs does not affect the potentiodynamic polarization curves, but significantly modifies the phase composition and structure of the formed coatings. The deposition current density of the alloy was also found to have an influence on the coating yield and the elemental and phase composition of the coatings studied.

For coatings deposited at a current density of 0.5 to 1.5 A/dm², Sn predominates in the coating composition up to 55% by weight. The anticorrosion properties of SnNi alloy-based coatings in an artificial sweat medium were investigated. It was found that the introduction of TiO_2NPs at a concentration of 1 g/l into the deposition electrolyte led to a significant reduction in the current density at the origin of the corrosion inhibition.

It has been found that the introduction of TiO_2NPs into the composition of the deposition electrolytes and, consequently, of the coatings produced, leads to an increase in the biocidal properties, both with and without UV radiation, which will allow these coatings to be used on objects in the public domain that come into frequent contact with people.

Author Contributions: Conceptualization, (A.C) and (A.T); methodology (H.P); validation, (A.T) and (Y.X); investigation, (M.V) (H.P) and (O. A); data curation, (O.A); writing—original draft, (H.P) and (V.B); formal analysis, (M.V), (H.P) and (V.B); writing—review and editing, (A.T) and (X.Y); supervision, (A.C) and (A.T). All authors have read and agreed to the published version of the manuscript.

Funding: This research was funded by grant of the Ministry of education of the Republic of Belarus, grant number 24-038 «Electrochemical production and physical-chemical properties of nickel-cobalt alloy».

Institutional Review Board Statement: Not applicable.

Informed Consent Statement: Not applicable.

Data Availability Statement: The data presented in this study are available on request from the corresponding author due to (specify the reason for the restriction).

Acknowledgments: The authors acknowledge the Ministry of education of the Republic of Belarus for supporting the achievement of this work.

Conflicts of Interest: The authors have no known competing financial interests or personal relationships that could have appeared to influence the work reported in this paper.

 doi:10.20944/preprints202409.0328.v1

References

1. Pop, A.B.; Iepure, G.; Titu, A.M.; Ravai-Nagy, S. Characterization and corrosion behavior of zinc coatings for two anti-corrosive protections: a detailed study. *Coatings.* **2023**, 13, 1460. https://doi.org/10.3390/coatings13081460.
2. Klapper, H. S.; Zadorozne, N. S.; Rebak, R. B. Localized corrosion characteristics of nickel alloys: a review. *Acta Metall. Sin. (Engl. Lett.)* **2017**, 30, 296–305. https//doi:10.1007/s40195-017-0553-z.
3. Shi, T.; Liang, J.; Li, X.; Zhang, C.; Yang, H. Improving the corrosion resistance of aluminum alloy by creating a superhydrophobic surface structure through a two-step process of etching followed by polymer modification. *Polymers* **2022**, 14, 4509. https://doi.org/10.3390/polym14214509.
4. Prando, D.; Brenna, A.; Diamanti, M.V. Corrosion of titanium: part 1: aggressive environments and main forms of degradation. *JABFM* **2017**, 15, e291-e302. https//doi:10.5301/jabfm.5000387.
5. Zhang, D.; Wei, B.; Wu, Z.; Wang, Z. A comparative study on the corrosion behaviour of Al, Ti, Zr and Hf metallic coatings deposited on AZ91D magnesium alloys. *Surf. Coat. Tech*. **2016**, 303, 94–102. https//doi: 10.1016/j.surfcoat.2016.03.079.
6. Shukla, P.; Awasthi, S.; Ramkumar, J.; Balani, K. Protective trivalent Cr-based electrochemical coatings for gun barrels. *J. Alloys Compd.* **2018**, 768, 1039–1048. https//doi:10.1016/j.jallcom.2018.07.170.
7. Marchewka, J.; Kołodziejczyk, E.; Bezkosty, P. Characterization of electrochemical deposition of copper and copper(I) oxide on the carbon nanotubes coated stainless steel substrates. *Sci. Rep.* **2023**, 13, 6786. https://doi.org/10.1038/s41598-023-33963-w.
8. Chen, M.; Liu, D.; Zi, B.; Chen, Y.; Liu, D.; Du, X.; Pan, H. Remarkable synergistic effect in cobalt-iron nitride/alloy nanosheets for robust electrochemical water splitting. *J. Energy Chem.* **2022**, 65, 405–414. https//doi:10.1016/j.jechem.2021.05.0.
9. Wei, B.; Legut, D.; Sun, S.; Wang, H. T.; Shi, Z. Z.; Zhang, H. J.; Zhang, R. F. Synergistic effect of solute and strain on the electrochemical degradation in representative Zn-based and Mg-based alloys. *Corros. Sci.* **2021**, 188, 109539. https//doi:10.1016/j.corsci.2021.109539.
10. Marinou, A.; Lekatou, A.G.; Xanthopoulou, G.; Vekinis, G. Electrochemical behavior of nickel aluminide coatings produced by CAFSY method in aqueous NaCl solution. *Coatings* **2022**, 12, 1935. https://doi.org/10.3390/coatings12121935.
11. Wu, P.; Xue, Z.; Yu, T.; Penkov, O.V. Transparent self-cleaning coatings: a review. *Coatings* **2023**, 13, 1270. https://doi.org/10.3390/coatings13071270.
12. Wang, S.; Wan, Y.; Song, N. Automatically generated datasets: present and potential self-cleaning coating materials. *Sci. Data* **2024**, 11, 146. https://doi.org/10.1038/s41597-024-02983-0.
13. Zheng, S.; Li, C.; Zhang, Y.; Xiang, T.; Cao, Y.; Li, Q.; Chen, Z. A General strategy towards superhydrophobic self-cleaning and anti-corrosion metallic surfaces: an example with aluminum alloy. *Coatings* **2021**, 11, 788. https//doi:10.3390/coatings11070788.
14. Su, F.; Yao, K. Facile Fabrication of superhydrophobic surface with excellent mechanical abrasion and corrosion resistance on copper substrate by a novel method. *ACS Appl. Mater. Interfaces* **2014**, 6, 8762–8770. https//doi:10.1021/am501539b.
15. Kharitonov, D. S.; Kasach, A. A.; Sergievich, D. S.; Wrzesińska, A.; Bobowska, I.; Darowicki, K.; Kurilo, I. I. Ultrasonic-assisted electrodeposition of Cu-Sn-TiO_2 nanocomposite coatings with enhanced antibacterial activity. *Ultrason. Sonochem.* **2021**, 75, 105593. https//doi:10.1016/j.ultsonch.2021.105.
16. Kasach, A. A.; Kharytonau, D. S.; Zharskii, I. M.; Kurilo, I. I. Electrocrystallisation of Cu-Sn-TiO_2 composite coatings in sulphuric acid electrolytes. *Condens. Matter and Interphases.* **2022**, 24, 220-226. https://doi.org/10.17308/kcmf.2022.24/9262.
17. Mitra, D.; Kang, E.-T.; Neoh, K. G. Antimicrobial copper-based materials and coatings: potential multifaceted biomedical applications. *ACS Appl. Mater. Interfaces* **2020**, 12, 21159-21182. https//doi:10.1021/acsami.9b17815.
18. Bharadishettar, N.; Bhat, K.U.; Bhat Panemangalore, D. Coating technologies for copper based antimicrobial active surfaces: a perspective review. *Metals* **2021**, 11, 711. https//doi:10.3390/met11050711.
19. O'Regan, B.C.; Grätzel, M. A low-cost, high-efficiency solar cell based on dye-sensitized colloidal TiO_2 films. *Nature* **1991**, 353, 737-740. https://doi:org/10.1038/353737a0.
20. Murashkevich, A.N.; Alisienok, O.A.; and Zharskii, I.M. Physicochemical and photocatalytic properties of nanosized titanium dioxide deposited on silicon dioxide microspheres, *Kinet. Catal.* **2011**, 52, 830. https//dos: 10.1134/S0023158411060140.

21. Jain, A.; Vaya, D. Photocatalytic activity of TiO_2 nanomaterial. *J. Chil. Chem. Soc.* **2017**, 62, 3683–3690. https//doi:10.4067/s0717-97072017000403683.
22. Mhadhbi, M.; Abderrazak, H.; Avar, B. Synthesis and Properties of Titanium Dioxide Nanoparticles. **2023**. 10.5772/intechopen.111577.
23. Freyre-Fonseca, V.; Téllez-Medina, D. I.; Medina-Reyes, E. I.; Cornejo-Mazón, M.; López-Villegas, E. O.; Alamilla-Beltrán, L.; Gutiérrez-López, G. F. Morphological and physicochemical characterization of agglomerates of titanium dioxide nanoparticles in cell culture media. *J. Nanomater.* **2016**, 1–19. https://doi.org/10:1155/2016/5937932.
24. Arumugam, C.; Velu, N.; Radhakrishnan, P.; Roy, V.A.L.; Anantha-Iyengar, G.; Lee, D.-E.; Kannan, V. Studies on the functional properties of titanium dioxide nanoparticles distributed in silyl–alkyl bridged polyaniline-based nanofluids. *Nanomaterials* **2023**, 13, 2332. https://doi.org/10.3390/nano13162332.
25. Mehraz, S.; Luo, W.; Swiatowska, J.; Bezzazi, B.; Taleb, A. Hydrothermal synthesis of TiO_2 aggregates and their application as negative electrodes for lithium–ion batteries: the conflicting effects of specific surface and pore size. *Materials* **2021**, 14, 916. https://doi.org/10.3390/ma14040916.
26. Praveen, B. M.; Venkatesha, T. V.; Naik, Y. A.; Prashantha K. Corrosion behavior of Zn-TiO_2 composite coatings. *Synth. React. Inorg. Met. Nano-Met. Chem.* **2007**, 37, 461-465, https//doi:10.1080/15533170701471216.
27. Kang, B.; Lan, D.; Liu, L.; Dang, R.; Yao, C.; Liu, P.; Ma, F.; Qi, S.; Chen, X. Antibacterial activity and bioactivity of Zn-Doped TiO_2 coating for implants. *Coatings* **2022**, 12, 1264. https://doi:org/10.3390/coatings12091264.
28. Makarava, I.; Esmaeili, M.; Kharytonau, D.S.; Pelcastre, L.; Ryl, J.; Bilesan, M.R.; Vuorinen, E.; Repo, E. Influence of CeO_2 and TiO_2 particles on physicochemical properties of composite nickel coatings electrodeposited at ambient temperature. *Materials* **2022**, 15, 5550. https//doi: 10.3390/ma15165550.
29. Baghery, P.; Farzam, M.; Mousavi, A. B.; Hosseini, M. Ni–TiO_2 nanocomposite coating with high resistance to corrosion and wear. *Surf. Coat. Technol.* **2010**, 204, 3804–3810. https//doi:10.1016/j.surfcoat.2010.04.06.
30. Thiemig, D.; Bund, A. Characterization of electrodeposited Ni–TiO_2 nanocomposite coatings. *Surf. Coat. Technol.* **2008**, 202, 2976–2984. https//doi:10.1016/j.surfcoat.2007.10.035.
31. Mozhgan, S.; Mahdi, M.; Seyed, M.E.; Mohammad, A. The role of TiO_2 nanoparticles on the topography and hydrophobicity of electrodeposited Ni–TiO_2 composite coating, *Surf. Topogr.: Metrol. Prop.* **2020**, 8, 025008. https//doi:10.1088/2051-672X/ab870a.
32. Birlik, I.; Ak Azem, N.F.; Toparli, M.; Celik, E.; Koc Delice, T.; Yildirim, S.; Bardakcioglu, O.; Dikici, T. Preparation and characterization of Ni–TiO_2 nanocomposite coatings produced by electrodeposition Technique. *Front. Mater.* **2016**, 3, 46. https//doi: 10.3389/fmats.2016.00046.
33. Rosolymou, E.; Karantonis, A.; Pavlatou, E.A. Effects of direct and pulse plating on the co-deposition of Sn–Ni/TiO_2 composite coatings. *Materials* **2024**, 17, 392. https://doi:org/10.3390/ma17020392.
34. Rosolymou, E.; Spanou, S.; Zanella, C.; Tsoukleris, D.S.; Kohler, S.; Leisner, P.; Pavlatou, E.A. Electrodeposition of photocatalytic Sn–Ni matrix composite coatings embedded with doped TiO_2 particles. *Coatings* **2020**, 10, 775. https://doi:org/10.3390/ma17020392.
35. Pyanko, A.V.; Makarova, I.V.; Kharitonov, D.S.; Makeeva, I.S.; Sergievich, D.S.; Chernik, A.A. Physicochemical and Biocidal Properties of Nickel–Tin and Nickel–Tin—Titania Coatings. *Prot. Met. Phys. Chem. Surf.* **2021**, 57, 88–95. https//doi: 10.1134/S2070205121010160.
36. Pyanko, A.V.; Makarova, I.V.; Kharitonov, D.S.; Makeeva, I.S.; Alisienok, O.A.; Chernik, A.A. Tin–Nickel–Titania Composite Coatings. *Inorg. Mater.* **2019**, 55, 568–575. https//doi: 10.1134/S002016851906013X.
37. Qader, I. Studying the Effect of TiO_2 Coating and Improving Biocompatibility of NiTiSn Biomedical Shape Memory Alloys. Thesis for: Ph.D. **2021**. https//doi:10.13140/RG.2.2.30078.92485.
38. Wan, C.; Zhang, L.; Liu, X. Corrosion assessment of Sn–Ni alloy coatings using neutral salt spray tests and electrochemical methods. *Int. J. Electrochem. Sci.* **2020**, 15, 26–38. https//doi: 10.20964/2020.01.20.
39. Wan, C.; Liu, X.; Ye, J. Tailorable deposition of Sn–Ni alloy from a pyrophosphate bath with an adjustable Sn:Ni molar ratio. *Surf. Coatings Technol.* **2019**, 369, 244–251. https://doi:org/10.1016/j.surfcoat.2019.04.070
40. Subramanian, B.; Mohan S.; Jayakrishnan, S. Selective area deposition of tin-nickel alloy-an alternative for decorative chromium plating. *J. Appl. Electrochem.* **2007**, 37, 219–224. https://doi:org/10.1007/s10800-006-9236-6.
41. La˘cnjevac, U.; Jovi´c, B.M.; Jovi´c, V.D. Electrodeposition of Ni, Sn and Ni–Sn alloy coatings from pyrophosphate-glycine bath. *J. Electrochem. Soc.* **2012**, 159, https//doi:D310. 10.1149/2.042205jes.

42. Rudnik E., The influence of sulfate ions on the electrodeposition of Ni-Sn alloys from acidic chloride-gluconate baths. *J. Electroanal. Chem.* **2014**, 726, 97–106. https://doi.org/10.1016/j.jelechem.2014.05.021.
43. Jalota, S.K. Tin–nickel alloy plating. *Met. Finish.* **1999**, 97, 319–322. https://doi.org/10.1016/S0026-0576(00)83092-5.
44. Kuznetsov, B.V.; Vorobyova, T.N.; Glibin, V.P. A Comparative study of tin-nickel alloys obtained by electroplating and casting. *Met. Finish.* **2013**, 111, 38–42. https://doi.org/10.1016/S0026-0576(13)70233-2
45. Lowenheim, F.A., Sellers, W.W., Carlin, F.X. The protective value of tin-nickel alloy deposits on steel. *J. Electrochem. Soc.* **1958**, 105, 338-346. https://doi:10.1149/1.2428841.
46. Shetty, S.; Hegde, A.C. Electrodeposition of Sn-Ni alloy coatings for water-splitting application from alkaline medium. *Metall. Mater. Trans. B.* **2017**, 48, 632–641. https://doi: 10.1007/s11663-016-0784-9.
47. Refaey, S.A.M.; Taha F.; Hasanin, T.H.A. Electrochemical behavior of Sn-Ni nanostructured compound in alkaline media and the effect of halide ions. *Appl. Surf. Sci.* **2004**, 227, 416-428. https://doi:10.1016/j.apsusc.2003.11.074.
48. Zhu, Y.; Liu, T.; Li, L.; Song, S.; Ding, R. Nickel-based electrodes as catalysts for hydrogen evolution reaction in alkaline media. *Ionics* **2018**, 24, 1121-1127. https://doi:10.1007/s11581-017-2270-z.
49. La˘cnjevac, U.C.; Jovi´c, V.D.; Jovi´c, B.M. Electrodeposition and characterization of Ni–Sn alloy coatings as cathodematerial for hydrogen evolution reaction in alkaline solutions. *ZAŠTITA Mater.* 2011, 52, 153–158.
50. Benea, L.; Danaila, E. Nucleation and growth mechanism of Ni/TiO_2 nanoparticles electro-codeposition. *J. Electrochem. Soc.* **2016**, 163, D655-D662. https://doi:10.1149/2.0591613jes.
51. Xue, Y.; Wang, S.; Zhao, G.; Taleb, A.; Jin, Y. Fabrication of NiCo coating by electrochemical deposition with high super-hydrophobic properties for corrosion protection. *Surf. Coat. Technol.* **2019**, 363, 352-361. https://doi.org/10.1016/j.surfcoat.2019.02.056.
52. Liang, C.; Liu, X.; Teng, F.; Li, Y.; Gao Sh. TiO_2/EP superhydrophobic composite coating with excellent mechanical and chemical stability. *Surf. Coat. Technol.* **2024**, 481, 130641. https://doi.org/10.1016/j.surfcoat.2024.130641.
53. Basavegowda, N.; Baek, K.-H. Multimetallic nanoparticles as alternative antimicrobial agents: challenges and perspectives. *Molecules* **2021**, 26, 912. https://doi.org/10.3390/ molecules26040912.
54. Gold, K.; Slay, B.; Knackstedt, M.; Gaharwar, A. K. Antimicrobial activity of metal and metal-oxide based nanoparticles. *Adv. Therap.* **2018**, 1, 1700033. https://doi:10.1002/adtp.201700033.
55. Celardo, I.; Pedersen, J. Z.; Traversa, E.; Ghibelli, L. Pharmacological potential of cerium oxide nanoparticles. *Nanoscale* **2011**, 3, 1411. https://doi:10.1039/c0nr00875c.
56. Arreche, R.; Bellotti, N.; Blanco, M.; Vázquez, P. Synthesis and characterization of zirconium oxides for use as antimicrobial additives in paints. *Proc. Mat. Sc.* **2015**, 9, 627–634. https://doi:10.1016/j.mspro.2015.05.039.
57. Nguyen, N.T.; Grelling, N.; Wetteland, C.L.; Rosario, R.; Liu, H. Antimicrobial activities and mechanisms of magnesium oxide nanoparticles (nMgO) against pathogenic bacteria, yeasts, and biofilms. *Sci. Rep.* **2018**, 8, 16260. https://doi: 10.1038/s41598-018-34567-5.
58. Liu, K.; Cheng, F.; Luo, Y.; Liu, L.; Wang, C.; Xie, K.; Luo, X. Porous single crystalline-like titanium dioxide monolith with enhanced photoelectrochemical performance. *Front. Mater* **2023**, 10, 1177093. https://doi:10.3389/fmats.2023.1177093.
59. Alshibeh, A. N.; Vacandio, F.; Vassalo, L.; Djenizian, T.; Coulomb, B.; Boudenne, J.-L. Effects of mode of preparation of titanium dioxide nanotube arrays on their photocatalytic properties: application to p-nitroaniline degradation. *Micro* **2023**, 3, 369–381. https://doi.org/10.3390/micro3010025.
60. Lowry, G.V.; Gregory, K.B.; Apte, S.C.; Lead, J.R. Transformations of nanomaterials in the environment. *Environ. Sci. Technol.* **2012**, 46, 6893−6899. https://doi: 10.1021/es300839e.
61. Oktar, F.N.; Yetmez, M.; Ficai, D.; Ficai, A.; Dumitru, F.; Pica, A. Molecular mechanism and targets of the antimicrobial activity of metal nanoparticles. *Curr. Top. Med. Chem.* **2015**, 15, 1583-8. https://doi:10.2174/1568026615666150414141601.
62. Ibáñez, J. A.; Litter, M. I.; Pizarro, R. A. Photocatalytic bactericidal effect of TiO_2 on Enterobacter cloacae. *J. Photochem. Photobiol. A* **2003**, 157, 81–85. https://doi:10.1016/s1010-6030(03)00074-1.
63. Wyszogrodzka, G.; Marszalek, B.; Gil, B.; Dorozynski, P. Metal-organic frameworks: mechanisms of antibacterial action and potential applications. *Drug Discovery Today* **2016**, http://dx.doi.org/10.1016/j.drudis.2016.04.009.

64. Abdal Dayem, A.; Hossain, M.; Lee, S.; Kim, K.; Saha, S.; Yang, G.-M.; Cho, S.-G. The role of reactive oxygen species (ROS) in the biological activities of metallic nanoparticles. *Int. J. Mol. Sci.* **2017**, 18, 120. https://doi:10.3390/ijms18010120.
65. Sandulescu, A.; Anastasescu, C.; Papa, F.; Raciulete, M.; Vasile, A.; Spataru, T.; Scarisoreanu, M.; Fleaca, C.; Mihailescu, C.N.; Teodorescu, V.; et al. Advancements on basic working principles of photo-driven oxidative degradation of organic substrates over pristine and noble metal-modified TiO_2. Model case of phenol photo oxidation. *Catalysts* **2021**, 11, 487. https://doi:org/ 10.3390/catal11040487.
66. Laxma Reddy, P. V.; Kavitha, B.; Kumar Reddy, P. A.; Kim, K.-H. TiO_2-based photocatalytic disinfection of microbes in aqueous media: A review. *Environ. Res.* **2017**, 154, 296–303. https://doi:10.1016/j.envres.2017.01.018.
67. Anandgaonker, P.; Kulkarni, G.; Gaikwad, S.; Rajbhoj, A. Synthesis of TiO_2 nanoparticles by electrochemical method and their antibacterial application. *Arab. J. Chem.* **2015**. https://doi:10.1016/j.arabjc.2014.12.015.
68. Younis, A.B.; Milosavljevic, V.; Fialova, T.; Smerkova, K.; Michalkova, H.; Svec, P.; Antal, P.; Kopel, P.; Adam, V.; Zurek, L.; Dolezelikova, K. Synthesis and characterization of TiO_2 nanoparticles combined with geraniol and their synergistic antibacterial activity. *BMC Microbiol.* **2023**, 23, 207. https://doi: 10.1186/s12866-023-02955-1.
69. Du, T.; Huang, B.; Cao, J.; Li, C.; Jiao, J.; Xiao, Z.; Wei, L.; Ma, J.; Du, X.; Wang, Sh. Ni nanocrystals supported on graphene oxide: antibacterial agents for synergistic treatment of bacterial infections. *ACS Omega* **2022**, 7, 18339–18349. https://doi.org/10.1021/acsomega.2c00508.
70. Yasuyuki, M.; Kunihiro, K.; Kurissery, S.; Kanavillil, N.; Sato, Y.; Kikuchi, Y. Antibacterial properties of nine pure metals: a laboratory study using Staphylococcus aureus and Escherichia coli. *Biofouling* **2010**, 26, 851–858. https://doi:10.1080/08927014.2010.527000.